JACS
JOURNAL OF THE AMERICAN CHEMICAL SOCIETY

Article

pubs.acs.org/JACS

Luminescent CdSe Superstructures: A Nanocluster Superlattice and a Nanoporous Crystal

Tetyana I. Levchenko,[†] Christian Kübel,[⊥] Bahareh Khalili Najafabadi,[†] Paul D. Boyle,[†] Carolyn Cadogan,[‡] Lyudmila V. Goncharova,[‡,§] Alexandre Garreau,[†] François Lagugné-Labarthet,[†,§] Yining Huang,*[,†,§] and John F. Corrigan*[,†,§]

[†]Department of Chemistry, The University of Western Ontario, London, Ontario N6A 5B7, Canada

[‡]Department of Physics and Astronomy, The University of Western Ontario, London, Ontario N6A 3K7, Canada

[§]The Centre for Advanced Materials and Biomaterials Research (CAMBR), The University of Western Ontario, London, Ontario N6A 5B7, Canada

[⊥]Institute of Nanotechnology and Karlsruhe NanoMicro Facility, Karlsruhe Institute of Technology, 76344 Eggenstein-Leopoldshafen, Germany

Supporting Information

ABSTRACT: Superstructures, combining nanoscopic constituents into micrometer-size assemblies, have a great potential for utilization of the size-dependent quantum-confinement properties in multifunctional electronic and optoelectronic devices. Two diverse superstructures of nanoscopic CdSe were prepared using solvothermal conversion of the same cadmium selenophenolate precursor $(Me_4N)_2[Cd(SePh)_4]$: the first is a superlattice of monodisperse $[Cd_{54}Se_{32}(SePh)_{48}(dmf)_4]^{4-}$ nanoclusters; the second is a unique porous CdSe crystal. Nanoclusters were crystallized as cubic crystals (≤0.5 mm in size) after solvothermal treatment at 200 °C in DMF. UV−vis absorption and PLE spectra of the reported nanoclusters are consistent with previously established trends for the known families of tetrahedral CdSe frameworks. In contrast to these, results of PL spectra are rather unexpected, as distinct room temperature emission is observed both in solution and in the solid state. The porous CdSe crystals were isolated as red hexagonal prisms (≤70 μm in size) via solvothermal treatment under similar conditions but with the addition of an alkylammonium salt. The presence of a three-dimensional CdSe network having a coherent crystalline structure inside hexagonal prisms was concluded based on powder X-ray diffraction, selected area electron diffraction and electron microscopy imaging. Self-assembly via oriented attachment of crystalline nanoparticles is discussed as the most probable mechanism of formation.

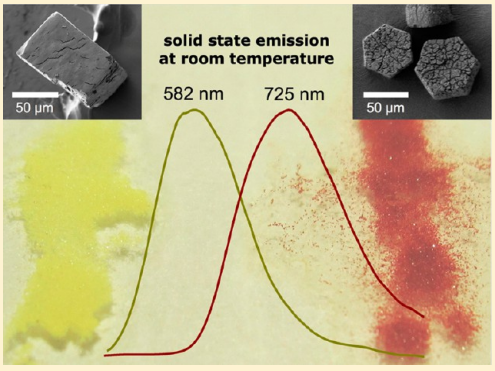

INTRODUCTION

The assembly of nanoscale building blocks (e.g., metallic or semiconductor nanoparticles) into ordered superstructures is a major goal of modern materials chemistry.[1−5] While exploiting the size-dependent quantum-confinement properties of nanoparticles, these superstructures can reach tens of micrometers in size, making them suitable for the creation of functional components for electronic and optoelectronic applications.[6−9]

Secondary structures can be built in a number of ways, depending, for instance, on the presence or absence of auxiliary linkers or the nature of the forces holding the superstructure together. Thus, uniform crystalline nanoparticles and nanoclusters stabilized by a surface passivating ligand shell can self-assemble into superlattices[10] held together by various noncovalent interactions and forces.[11] Among them, crystals of monodisperse group 12-16 semiconductor nanoclusters stabilized by phenyl chalcogenolate ligands are well-ordered (cubic) superlattices formed via Coulomb or van der Waals interactions between neighboring nanoclusters. The largest structurally characterized examples of such nanoclusters are $[Cd_{54}Se_{32}(SPh)_{48}(H_2O)_4]^{4-}$ and $[Cd_{54}S_{28}(SPh)_{52}(dmf)_4]$, containing water and *N*,*N*′-dimethylformamide (*dmf*) ligands along with PhS^-.[12,13] The connection between building blocks in superlattices is typically reversible, even with a relatively stronger cluster−cluster interaction, such as hydrogen bonding (e.g., between $[Cd_{32}S_{14}(SCH_2CH(OH)CH_3)_{36}(H_2O)_4]$ nanoclusters in a double-layer three-dimensional superstructure).[14] Thus, dissolving the crystals can disassemble the superlattices.

Much stronger cluster−cluster interactions include the covalent assembly of inorganic frameworks without auxiliary linkers into one-, two- and three-dimensional superstructures. For crystalline faceted nanoscale constituents, direct covalent assembly is possible by vertex-sharing or face fusion. Thus, the chalcogenolate stabilizing ligands at the vertices of metal chalcogenide nanoclusters can also act as bridging intercluster

Received: October 6, 2016
Published: January 13, 2017

DOI: 10.1021/jacs.6b10490
J. Am. Chem. Soc. 2017, 139, 1129−1144

linkers between outer metal atoms, resulting in the formation of extended, ordered structures.[15] Examples of one-point cluster−cluster connections formed by vertex-sharing include $[Cd_{17}S_4(SPh)_{26}(py)]$ (*py* = pyridine) connected in one-dimensional chains;[13] two-dimensional frameworks of six-member rings formed by $[Cd_{17}S_4(SPhMe\text{-}4)_{27}(SH)]^{2-}$;[16] and $[Cd_{17}S_4(SCH_2CH_2OH)_{26}]$ crystallizing as a three-dimensional superstructure with the double diamond topology.[17]

In the case of face fusion, superstructure formation is often mediated by the spontaneous arrangement of adjacent crystalline primary building blocks sharing a common crystallographic orientation.[18−21] Next, new covalent bonds form, joining certain facets of crystalline particles and resulting in the irreversible assembly of superstructures with complex morphology and single-crystal-like properties (oriented attachment mechanism).[22] It has been proposed that, in many cases, superstructure formation by face fusion is enabled by adsorption−desorption equilibria in the stabilizing (organic) shell on primary building blocks.[23] Surfactants or macromolecules showing facet-specific adsorption may play a decisive role in triggering fusion and determining the geometry of the resulting superstructure by making certain crystalline facets reactive. This formation mechanism has been frequently observed and is well understood in the nonclassical crystallization of metal chalcogenide one-dimensional superstructures (i.e., nanowires or nanorods from preformed nanoparticles).[24−27] There are significantly fewer examples of two-dimensional superstructures formed through face fusion.[28,29]

Hybrid, covalently assembled superstructures, in which nanodimensional inorganic building blocks are joined by polydentate organic ligands, form a large, diverse family with a vast variety of structural types.[30,31] Of particular interest among recently reported superstructures are coordination polymers,[32] in which bi-, tri- or tetradentate N-containing (e.g., pyridyl- or imidazole-based) ligands attached to vertices create ordered links between tetrahedral metal chalcogenide nanoclusters.[33,34] Thus, $[Cd_{32}S_{14}(SPh)_{36}L_{4/2}]$ can be assembled by the flexible, bidentate ligand L = 4,4′-trimethylenedipyridine in either one-dimensional, doubly bridged chains[35] or two-dimensional superstructures with alternating singly and doubly bridged clusters in layers.[36]

The collective properties of nanocluster assemblies are partly inherited from their constituent cluster frameworks and partly arise from synergistic interactions between superstructure components. Thus, emerging properties may be induced by the electronic, plasmonic and magnetic coupling between building blocks.[37]

Here, we report the preparation of two distinct regular superstructures using the same mononuclear cadmium selenophenolate precursor. First, a superlattice of monodisperse $(Me_4N)_4[Cd_{54}Se_{32}(SePh)_{48}(dmf)_4]$ nanoclusters (**1**) was crystallized as cubic crystals after solvothermal treatment at 200 °C in DMF. A second superstructure, porous CdSe crystal (**2**), was isolated as red hexagonal prisms among the products of the solvothermal treatment under similar conditions but in the presence of cetyltrimethylammonium bromide (CTAB). To illustrate the structures of both materials, the results of single-crystal and powder X-ray diffraction, selected area electron diffraction (SAED) and electron microscopy characterization are discussed. Particular attention is paid to evaluation of the optical properties (including emission) of the two superstructures. Crystallization by oriented attachment of nanoparticles is proposed as the most probable formation mechanism for porous CdSe crystal.

RESULTS AND DISCUSSION

1. Superlattice of Large CdSe Nanoclusters. Although cadmium chalcogenolates are among the most widely used single source precursors for the preparation of CdE (E = S, Se, Te) nanoparticles and molecular nanoclusters, only a few explored synthetic routes involved mononuclear $[Cd(EPh)_4]^{2-}$.[38] In our experiments, heating solutions of colorless $(Me_4N)_2[Cd(SePh)_4]$ in DMF at 200 °C for 1 day results in a solution color change to orange-yellow as solvothermal conversion of the precursor occurs with formation of polynuclear cadmium selenophenolate species. Visual observations were supported by UV−vis absorption spectra of the reaction solutions, showing the presence of intense excitonic absorption bands (see discussion below), which is evidence for the formation of monodisperse species of a particular size. Rapid crystallization occurs from these solutions after opening reaction autoclaves, yielding large (up to 0.5 mm in length), transparent, yellow, cubic crystals (**1**), which are typically found to be cracked to some extent.

1.1. Structure and Morphology. Characterization using single-crystal X-ray diffraction shows that **1** represents a cubic superlattice of monodisperse nanoclusters possessing a tetrahedral $Cd_{54}Se_{80}$ core (Figure 1). This core is built up

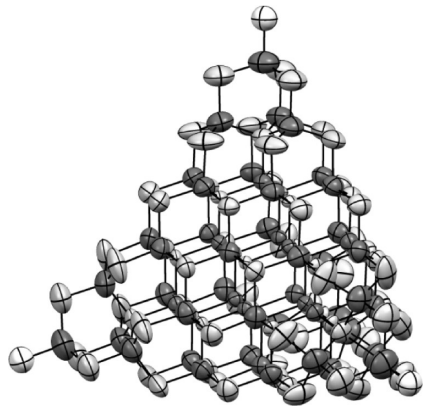

Figure 1. $Cd_{54}Se_{80}$ core structure of **1**. Cd atoms are shown as dark gray; Se, light gray. Four O atoms at vertexes of the tetrahedron (shown white) belong to *dmf* ligands.

from a relatively large fragment of a regular cubic CdSe framework and four hexagonal CdSe cages in four corners (completing the shape of the tetrahedron): a new member of capped supertetrahedral cluster family, represented by previously reported $[Cd_{17}S_4(SPh)_{28}]^{2-}/[Cd_{17}Se_4(SePh)_{28}]^{2-}$; $[Cd_{32}S_{14}(SPh)_{36}(dmf)_4]/[Cd_{32}Se_{14}(SePh)_{36}(PPh_3)_4]$; and $[Cd_{54}S_{28}(SPh)_{52}(dmf)_4]/[Cd_{54}Se_{32}(SPh)_{48}(H_2O)_4]^{4-}$ with a similar build-up principle.[12,13,39−42] In the crystalline core of nanoclusters **1**, the edge length of the tetrahedron is 2.17 nm (taking the center of the Cd−O bond as the vertex). The height of such a tetrahedron is 1.77 nm and the diameter of the sphere having the same volume as this tetrahedron (the equivalent spherical diameter) is 1.32 nm; both values can be used for comparison with nanoparticles of different shapes.[43] Molecular nanoclusters **1** form a superlattice in the space group $P\bar{4}3m$ with a unit cell parameter 24.412(6) Å (see SI *Table S1*), very close to the cell constant of previously reported

DOI: 10.1021/jacs.6b10490
J. Am. Chem. Soc. 2017, 139, 1129−1144

$[Cd_{54}Se_{32}(SPh)_{48}(H_2O)_4]^{4-}$ which contains a thiolate ligand shell ($P23$ and 24.065 6(7) Å, respectively).[12] Substantial disorder of the surface organic ligands (which is often observed in single-crystal structures based on large monodisperse CdS or CdSe nanoclusters; see, for instance, references 12, 13, 44) did not allow for full characterization of the stabilizing shell of **1** by single-crystal X-ray diffraction. However, a set of auxiliary analyses, including Raman spectroscopy, indicates $PhSe^-$ as surface-stabilizing ligand (see discussion below). The distinct feature of the superlattice in **1** is the presence of large intercluster voids (~30% of unit cell volume was calculated assuming phenyl rings present), not containing any heavy atoms but only crystallization solvent molecules and/or charge-balancing species.

PXRD patterns for **1**, obtained for freshly prepared crystals (with some mother liquor) ground under paraffin oil, match the corresponding patterns calculated using single-crystal X-ray diffraction data (Figure 2, patterns *ii* and *i*, respectively),

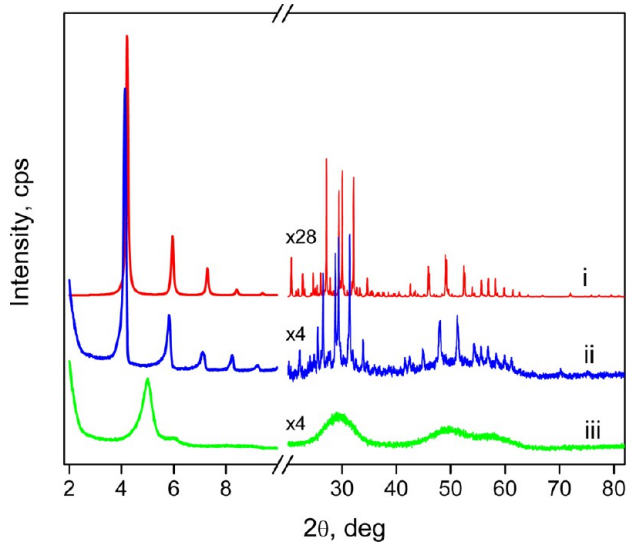

Figure 2. Measured (fresh material in paraffin oil, *ii*; dried material, *iii*) and simulated (*i*) powder X-ray diffraction patterns (Co Kα radiation) for **1**. Pattern *ii* was corrected for paraffin oil background. Wide-angle region is scaled ×4 for patterns *ii* and *iii*, and ×28 for the pattern *i*; the data are shown with *Y*-axis offset for clarity.

confirming phase purity of the material. A small shift toward low angles (2θ 0.1−0.2°) of the reflections for measured diffraction patterns versus calculated ones was observed previously (see, for example, ref 45) and can be explained by the effect of thermal expansion (PXRD measurements done at room temperature vs 110 K for single-crystal data collection for **1**). In the low-angle region of PXRD patterns, of note is a strong and sharp reflection at 2θ 4.13°, together with much weaker and broader ones at 5.82, 7.11 and 8.25° (in accordance with primitive cubic unit cell). From the position of the first reflection, the corresponding interplanar spacing d of 2.48 nm was calculated using the Bragg equation. In the wide-angle region, sharp and quite intense peaks (matching with calculated values) are displayed together with very broad and unresolved ones.

Upon isolation and vacuum-drying of **1**, initially large crystals fracture into smaller ones; this process may reflect substantial changes in the superlattice, most probably due to removal of crystallization solvent. First observed by the naked eye and optical microscopy (Figure 3*a*), the cracking spans to the micrometer scale, with multiple defects in block fragments of the dried material **1** seen on its SEM images (Figure 3*b*). Despite high electron beam sensitivity of **1**, TEM images were obtained for thin areas close to the crystal edge (wet preparation method), showing projections of the continuous domains of ordered superlattice of monodisperse nanoclusters (with the CdSe core appearing as darker regions and the $PhSe^-$ shell as brighter spaces) with a measurable lattice parameter 2.05 nm (Figure 3*c*). This value for the dried material **1** is substantially smaller than a unit cell parameter 2.48 nm, found from powder X-ray diffraction data for solvated crystals of **1**. Low-angle SAED reflections of **1** are in agreement with the presence of superlattice with d-spacing close to that measured from TEM (Figure 3*c*, *inset*). PXRD measurements on dried samples of **1** (see Figure 2, pattern *iii*) confirmed formation of a new superlattice arrangement as well: from the position of the first low-angle reflection at 2θ 5.00° a corresponding interplanar spacing d of 2.05 nm was calculated. Quantitative comparison of the peak intensities for fresh versus dried samples of **1** is complicated, as different sample preparation techniques were used for collecting the diffraction patterns. Overall, however, the intensity of low-angle peaks for the dried material **1** is noticeably lower and the peaks themselves are less sharp, reflecting a decrease of order upon superlattice rearrangement. Although the broad and low intensity nature of the weak, low-angle peaks (around ~6, 8 and 9°) complicates the analysis, a (new) hexagonal superlattice can

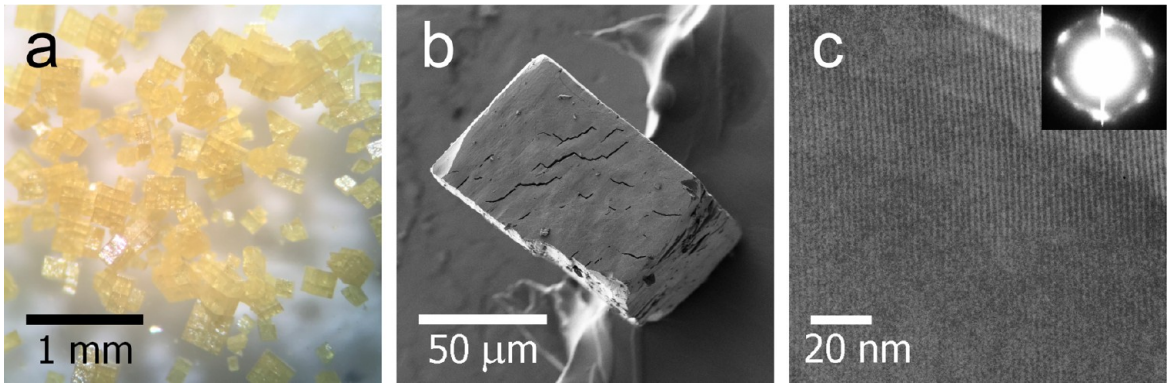

Figure 3. Microscopy images of dried **1**: optical micrograph, taken by a digital camera through the objective of an optical microscope (*a*), SEM (*b*) and HRTEM (*c*). Inset: low-angle SAED reflections of **1**.

DOI: 10.1021/jacs.6b10490
J. Am. Chem. Soc. 2017, 139, 1129−1144

be suggested. TEM and SAED data are in agreement with such interpretation. In the wide-angle region of the PXRD patterns for dried **1** (Figure 2, pattern *iii*), only broad peaks are found (as previously noted for dried $[Cd_{32}Se_{14}(SePh)_{36}(PPh_3)_4]$ superlattice);[46] these do nonetheless illustrate the relation of the internal structure of **1** with bulk cubic and hexagonal structures of CdSe (see below). The breadth of the wide-angle peaks in the PXRD patterns for dried **1** (Figure 2, pattern *iii*) is substantially different from PXRD patterns for freshly prepared crystals **1**, where both sharp and broad peaks appear (Figure 2, pattern *ii*).

The broadening of peaks in a diffraction pattern of nanoscale crystalline materials is typically attributed to the effect of crystallite size (after accounting for other sources of broadening, e.g., instrumental factors).[47,48] Indeed, calculations of the mean size of the crystalline domains using the Scherrer equation for the dried material **1** give a value of 1.55 nm, which is close to the size determined from X-ray crystallography (e.g., tetrahedron height and the equivalent spherical diameter are 1.77 and 1.32 nm, respectively). The absence of sharp reflections in the wide-angle region of PXRD patterns for the dried material **1** is consistent with the superlattice rearrangement with decrease in its long-range order.

X-ray diffraction (single-crystal and powder) and electron microscopy provide concrete data for both the nature of the individual building blocks and their secondary structure in material **1**: monodisperse nanoclusters with a tetrahedral $Cd_{54}Se_{80}$ core form a primitive cubic superlattice. We observed that crystallization begins only after opening (to inert atmosphere) the autoclave in which the solvothermal synthesis was performed. This is unusual, because, typically, the main reaction product crystallizes either in the process of cooling reaction solutions to room temperature or immediately after the cooling is finished. It is possible that release of gaseous byproducts from solvothermal conversion (e.g., NMe_3) upon opening the autoclave changes some properties of the solution and thus triggers crystallization of material **1**. Upon isolation and drying, the ordered superlattice in **1** persists but its parameters are found to be substantially different from those of the freshly isolated material. Thus, rearrangement from cubic to hexagonal superlattice with a unit cell length decrease for 17% is observed probably due to removal of crystallization solvent. As far as we know, no such significant structure rearrangement was previously followed using PXRD for metal chalcogenide nanoclusters. The rearrangement is expected to be the distinctive feature of the superlattices of large nanoclusters, with high (cubic) symmetry and spacious intercluster voids.

1.2. Ligand Shell Composition. Analysis of the stabilizing organic shells of the nanoparticles (including ligands identification and quantification) is often a complex task which requires a set of complementary analytical techniques to be applied.[49] Raman spectroscopy allowed extending characterization of material **1** as observed bands can be assigned to the vibrations of bonds in both the $Cd_{54}Se_{80}$ core and ligand shell. Thus, in the low-frequency region of Raman spectra of **1** a broad, medium-strong band at 201 cm^{-1} (SI *Figure S1*) appears, close to the one of the most intense bands in bulk CdSe at 210 cm^{-1} (the bulk longitudinal optical phonon mode)[50] and can be assigned to the stretching vibrations of interior Cd−Se bonds[46] in the $Cd_{54}Se_{80}$ core. The broadness and asymmetry (a low-frequency shoulder at ∼193 cm^{-1}) of the peak can be related with a contribution from surface optical phonon mode or other confinement-induces effects.[51,52] The size dependence of the optical phonon frequency of nanoscale crystalline solids was previously described theoretically[53,54] and observed experimentally as a shift to lower wavelength with CdSe nanoparticle size decrease (see, for instance, refs 55−58). Several strong bands in characteristic aromatic areas (e.g., at 3052 cm^{-1} due to aromatic C−H stretch vibrations and 1574 cm^{-1} due to aromatic C−C stretch vibrations) as well as the medium-strong band at 666 cm^{-1} due to Se−C stretch vibrations[59] are in agreement with $PhSe^-$ ligands present on the surface of **1**. Only weak bands (e.g., at 2992 and 2940 cm^{-1}) can be found in the area characteristic for aliphatic C−H stretching. The weak aliphatic signal may originate from residual lattice solvent (DMF) or coordinated *dmf* in the stabilizing shell of nanoclusters **1** at four apexes similar to previously reported cadmium sulfide nanoclusters $[Cd_{32}S_{14}(SPh)_{36}(dmf)_4]$ and $[Cd_{54}S_{28}(SPh)_{52}(dmf)_4]$.[13,41] Also, charge-balancing species (e.g., $(Me_4N)^+$) may be present in crystalline packing of anionic nanoclusters to achieve overall neutral system, as was reported for $[Cd_{54}Se_{32}(SPh)_{48}(H_2O)_4]^{4-}$.[12]

Using energy dispersive X-ray (EDX) spectroscopy for the analysis of cubic crystals of **1**, the Cd/Se atomic ratio is found to be 0.74:1 which is reasonably close to the 0.675:1 expected for both $(Me_4N)_4[Cd_{54}Se_{32}(SePh)_{48}(dmf)_4]$ and $[Cd_{54}Se_{28}(SePh)_{52}(dmf)_4]$. Elemental analysis (C, H, N, S), TGA and mass spectrometry (see SI *Figures S2−S3* and discussion of results thereby) are in agreement with these stoichiometries as well. Overall, the results of auxiliary analyses are consistent with molecular formula $(Me_4N)_4[Cd_{54}Se_{32}(SePh)_{48}(dmf)_4]$ for **1**, whereas neutral $[Cd_{54}Se_{28}(SePh)_{52}(dmf)_4]$ nanocluster cannot be excluded.

1.3. Optical Properties. The fragments of cubic crystals of dried **1** display distinct luminescence in the solid state; a combination of optical microscopy and luminescence imaging confirms that emission is clearly observed at room temperature, homogeneously distributed from every part of the sample (Figure 4). The confocal fluorescence microscopy images are

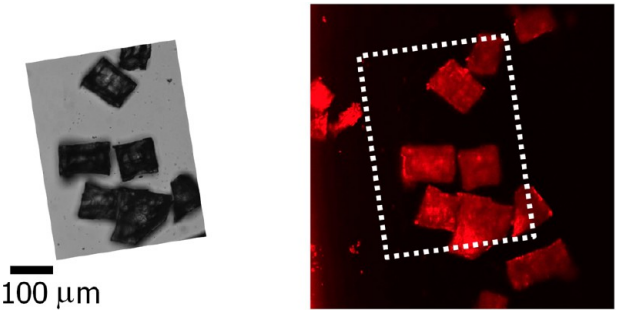

Figure 4. Transmission optical (*left*) and confocal fluorescent microscopy (*right*) images of fragments of cubic crystals of **1**. The confocal fluorescence microscopy images are pseudocolored red.

pseudocolored red; the real color of emitted light is discussed below. Because an absence of room temperature emission was reported for related, smaller cadmium chalcogenide nanoclusters both in the solid state and in solution,[41,46] the optical properties of **1** were examined more closely using UV−vis, photoluminescence (PL) and photoluminescence excitation (PLE) spectroscopy.

Similar to previously reported cadmium chalcogenide nanoclusters, clusters **1** can be dissolved in some polar solvents, breaking interactions between nanoclusters in the superlattice

DOI: 10.1021/jacs.6b10490
J. Am. Chem. Soc. 2017, 139, 1129−1144

while leaving intact individual frameworks.[12,41] It also was reported previously that keeping cadmium chalcogenide nanoclusters dissolved in strongly coordinating solvent for >24 h or performing additional treatments, like sonication or heating of the solution, may modify the nanoclusters themselves. The changes may vary from partial ligand exchange[60] to significant cluster core rearrangement.[61] To avoid any changes in nanocluster composition, all measurements of optical properties were done for solutions prepared by stirring at room temperature immediately after dissolving crystalline samples.

The UV−vis absorption spectra of solutions of **1** in DMF (Figure 5) show the presence of sharp and narrow excitonic features. The lowest energy absorption band is observed at 410 nm (fwhm 22 nm). The peak width for monodisperse nanoclusters in **1** is related with effects other than distribution of sizes, e.g., electron−phonon coupling or trapping to surface states.[62] The peaks at shorter wavelengths (i.e., 376 and ∼310 nm; fwhm ∼40 and ∼30 nm, revealed upon deconvolution; see SI *Figure S4*) are attributed to the excited states of the excitons on the same CdSe nanoclusters. The first two absorption peaks are assigned to $1S(e)-1S_{3/2}(h)$, $1S(e)-2S_{3/2}(h)$, transitions, respectively; whereas the third peak can be assigned to the $1P(e)-1P_{3/2}(h)$, $1S(e)-2S_{1/2}(h)$ or $1P(e)-1P_{1/2}(h)$ transitions or their combination.[63,64] The ambiguity in assignment of the higher energy peaks is related with the size dependence of relative positions and intensities of the transitions in the strong confinement regime (when the particle radius is a few times smaller than the exciton Bohr radius, which is 5.6 nm for CdSe).[64] On the basis of the empirical formula proposed by Yu et al.,[65] the lowest energy absorption band at 410 nm for **1** would correspond to (spherical) CdSe particles with average diameter 1.64 nm, which is close to the parameters derived using X-ray single-crystal (1.32−1.77 nm) and powder diffraction (1.55 nm) data.

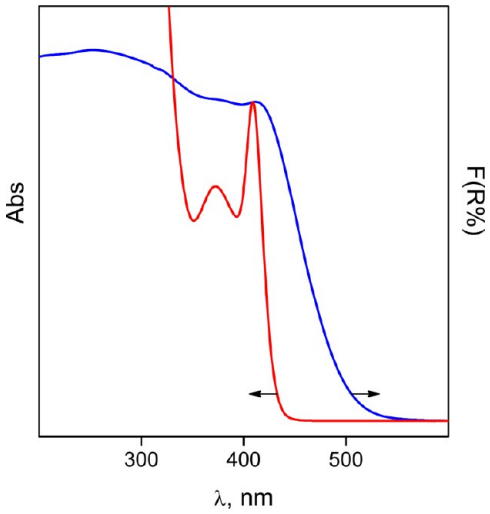

Figure 5. UV−vis absorption spectrum of **1** dissolved in DMF (normalized) and diffuse reflection spectrum of solid material **1** (processed using the Kubelka−Munk function and normalized).

The effect of cluster composition (for a given $Cd_xE_y(E'Ph)_z$ cluster size, where E, E′ = S, Se, Te) was systematically followed previously for smaller frameworks. In the case of dichloroethane solutions of $[Cd_{10}E_4(E'Ph)_{12}L_4]$ (L = P^nPr_3 or P^nPr_2Ph) and acetonitrile solutions of $[Cd_{17}E_4(E'Ph)_{28}]^{2-}$, the lowest-energy excitonic peak shows a red shift upon changing from sulfur (E = E′ = S) to the heavier chalcogenide and chalcogenolate ligands through various mixed species (e.g., E = Se, E′ = S) to pure selenium- or tellurium-containing clusters (E = E′ = Te).[45,66] Along this line, a shift toward longer wavelength is observed from $[Cd_{54}S_{32}(SPh)_{48}(H_2O)_4]^{4-}$ through $[Cd_{54}Se_{32}(SPh)_{48}(H_2O)_4]^{4-}$[12] to **1** (i.e., $[Cd_{54}Se_{32}(SePh)_{48}(dmf)_4]^{4-}$), with the low-energy excitonic peak positions found at 353, 393 and 410 nm, respectively, in DMF solutions.

The main features in the UV−vis absorption spectrum of **1** in DMF essentially match with those of reactions solutions prior to crystallization (i.e., a distinct peak at ∼414 nm with shoulder at ∼376 nm, see SI *Figure S5*), although the latter is broader, slightly red-shifted and has a distinct tail to longer wavelengths can be discerned. After crystallization is complete, the peak at ∼414 nm and shoulder at ∼376 nm are no longer present in the spectra of the mother liquor (SI *Figure S5*). However, two weak, broad bands at 438 and ∼465 nm become more visible after crystallization. These remaining features suggest that larger CdSe species (probably having a distribution of sizes) are also present. Due to a lack of monodispersity, these species would not proceed further (crystallize), whereas nanoclusters of **1** crystallize into their superlattice, forming a pure solid phase.

Although material **1** dissolves most readily in DMF (solubility ∼6 mg/mL), it also can be dissolved in acetonitrile (solubility <0.1 mg/mL). The UV−vis absorption spectrum of **1** dissolved in acetonitrile is essentially identical to that in DMF (SI *Figure S4*). However, the lower absorption onset for this solvent itself allowed for another band at 245 nm to be observed, associated with transitions within the aryl ring of the surface $PhSe^-$ ligands. Unlike highly coordinating DMF in which cluster core rearrangement was reported previously for smaller CdS and CdSe nanoclusters, acetonitrile is less likely to cause such changes. An absence of any significant difference in absorption bands position or width in the UV−vis spectra of **1** in DMF and acetonitrile suggests that the structures do not change considerably upon dissolution. In agreement with this, mass spectra of **1** dissolved in DMF and acetonitrile show the presence of identical ionic species. The molar extinction coefficients ε at the lowest-energy absorption peak was found ∼127 000 $M^{-1}\cdot cm^{-1}$ in DMF, suggesting that the first transition is strongly allowed. The value of ε for **1** is comparable with those reported previously for smaller cadmium chalcogenide nanoclusters, for instance, 84 500 $M^{-1}\cdot cm^{-1}$ in THF solution for $[Cd_{32}S_{14}(SPh)_{36}(dmf)_4]$[41] and 52 000 $M^{-1}\cdot cm^{-1}$ in acetonitrile solution for $[Cd_{32}Se_{14}(SePh)_{36}(PPh_3)_4]$.[43] Strong size dependence of ε at the lowest-energy absorption peak was also found previously for crystalline CdS, CdSe and CdTe nanoparticles, which increases supralinearly (i.e., departing from linear in a concave upward manner) with increasing particle diameter.[65,67] The fact that the position of the absorption bands is insensitive to change of solvent polarity (as with transition from DMF to acetonitrile, relative polarity changes from 0.386 to 0.460)[68] indicates that the ground state or the corresponding excited state have a vanishingly small dipole moment. This observation, together with the large oscillator strength, is in agreement with characteristics of an excitonic transition.[41]

In the UV−vis diffuse reflectance spectra of solid **1**, the lowest-energy absorption peak is broader, and an onset of the peak is shifted toward a longer wavelength in comparison to solution data (Figure 5). A similar relation between the UV−vis

DOI: 10.1021/jacs.6b10490
J. Am. Chem. Soc. 2017, 139, 1129−1144

absorption spectra of solid and dissolved material was reported previously for smaller CdS nanoclusters and attributed to weak cluster−cluster interaction present in the superlattice.[14,41]

Low-temperature (T = 77 K) emission spectra of **1** in DMF show a distinct and rather broad (fwhm 72 nm) band at 509 nm (Figure 6). This emission maximum is red-shifted in comparison with the previously reported emission for smaller $[Cd_{32}Se_{14}(SePh)_{36}(PPh_3)_4]$, where the emission band was observed at 480 nm (fwhm ∼65 nm) while measured in Nujol suspension at T = 8 K.[46] The peak in the emission spectrum of **1** is asymmetric, with a tail toward higher wavelengths, and the peak shape and position changes a little (<8 nm for the latter) when the wavelength is varied from the red edge to blue excitation (SI *Figure S6*). This lack of wavelength dependence provides additional evidence for the purity and homogeneity[69,70] of the species **1**, having the same nature of the emitting state. Several peaks are resolved in the corresponding low-temperature photoluminescence excitation spectra: a distinct narrow absorption band at 394 nm and weaker ones at 368 and 324 nm (Figure 6). These bands match the excitonic transitions observed in UV−vis absorption spectra of **1** (Figure 5).

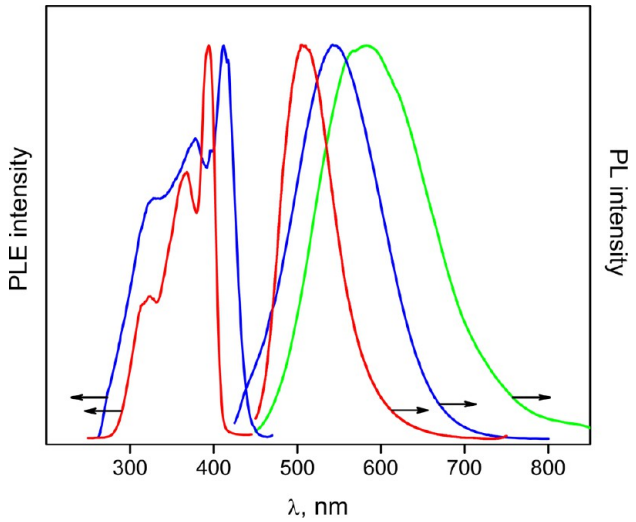

Figure 6. Normalized PL and PLE spectra of **1** dissolved in DMF, obtained at 77 K (red) and at room temperature (blue); PL spectrum of **1** in solid state, obtained at room temperature (green). For the spectra in solution, the excitation wavelength for PL spectra corresponds to the low-energy band in corresponding PLE; the monitoring wavelength for PLE spectra−to the PL maximum. For solid state PL spectrum, the excitation wavelength was 405 nm.

Unlike previously reported smaller CdSe nanoclusters (for which no detectable emission was observed above 150−200 K due to fast nonradiative decay processes),[46] solutions of **1** also exhibit prominent emission at room temperature. Here, emission is observed at 545 nm, shifted toward a longer wavelength in comparison to the low-temperature spectrum, with a larger fwhm of 123 nm (Figure 6). Such increased line width can be explained in terms of thermal broadening. In comparison with the low-temperature data, room temperature emission also has a weak shoulder at shorter wavelength (∼440 nm), which suggests that competing transitions may take place for solutions of **1** at room temperature. With increases in concentration of **1** in DMF solutions, the intensity of emission increases as well, whereas peak position, width, and shape remain the same (SI *Figure S7*).

The room-temperature excitation spectrum shows a distinct, relatively narrow absorption band at 412 nm and weaker ones at 378 and ∼328 nm; all peaks are red-shifted in comparison to those in the low-temperature spectra (Figure 6). With an increase in the concentration of **1** in DMF, not only does the intensity of the excitation band increase but the ratio between the three absorption bands also changes and additional narrow features (i.e., at 418 and 397 nm denoted by asterisk * in SI *Figure S7*) gradually become resolved. The substructure of the low-energy band in PLE spectra was reported previously for CdSe nanoparticles and assigned to the band-edge exciton splitting (LO-phonon substructure) due to the particle's crystalline structure, nonspherical shape and electron−hole exchange interaction enhanced by quantum confinement.[63,71,72] It is noteworthy that resolving such fine structure in the PLE spectra of CdSe nanoparticles with sizes comparable to the size of **1** (e.g., in examined series of samples the smallest mean effective diameter was ∼3 nm from TEM vs the tetrahedron height for **1** 1.77 nm) required special experiments to be conducted (e.g., transient differential absorption or fluorescence line narrowing spectroscopy at 10 K) to reduce line-broadening inhomogenity (by size, shape and surface chemistry) of the nanoparticles.[63,71−74] In contrast, in the room temperature PLE spectra of monodisperse nanoclusters **1** the additional, narrow features are well resolved.

Solid-state emission spectra of **1** show a distinct broad (fwhm 151 nm) band at 582 nm (Figure 6), supporting previous observations using confocal fluorescent microscopy and confirming that pronounced green emission at room temperature is inherent to material **1** itself, and does not come from any new species arising from possible changes in solution. The red shift of the emission maximum in the solid state, in comparison to its position for **1** in DMF solution (both at room temperature), is in agreement with the weak cluster−cluster interactions present in the superlattice.

Emission bands in the PL spectra of CdSe nanoclusters and nanoparticles, reported previously, were generally assigned to (1) band edge fluorescence or (2) deep trap emission.[75,76] Emission of both types can also be observed in the same spectrum (see, for instance, ref 77). The band edge emission (recombination of free charge carriers) is characterized by narrow peak shape, a small red shift from the absorption band, and a short lifetime. For both low and room temperature PL/PLE measurements for **1**, the emission is considerably red-shifted from the lowest energy excitation: by 115 and 133 nm, respectively. A comparable shift (∼107 nm) was observed previously in PL/PLE spectra of $[Cd_{32}Se_{14}(SePh)_{36}(PPh_3)_4]$ obtained in Nujol suspension at T = 8 K.[46] On the basis of the broad line width of the emission and the significant shift to the red, the emission observed for **1** likely originates from the radiative recombination of charge carriers, trapped on the surface selenophenolate $PhSe^-$ ligands ("trapped emission"), previously suggested for smaller nanoclusters.[43,46] An assignment of the emission to transitions related with phenylchalcogenolate ligands was further supported by a significant blue shift of the PL maximum for the nanoclusters with the same size and core composition but having thiophenolate vs selenophenolate ligands.[78] The corresponding excited state is not detected in the absorption spectrum because it has a low oscillator strength (as a forbidden transition). For monodisperse nanoclusters, the broad line width for the emission

DOI: 10.1021/jacs.6b10490
J. Am. Chem. Soc. 2017, 139, 1129−1144

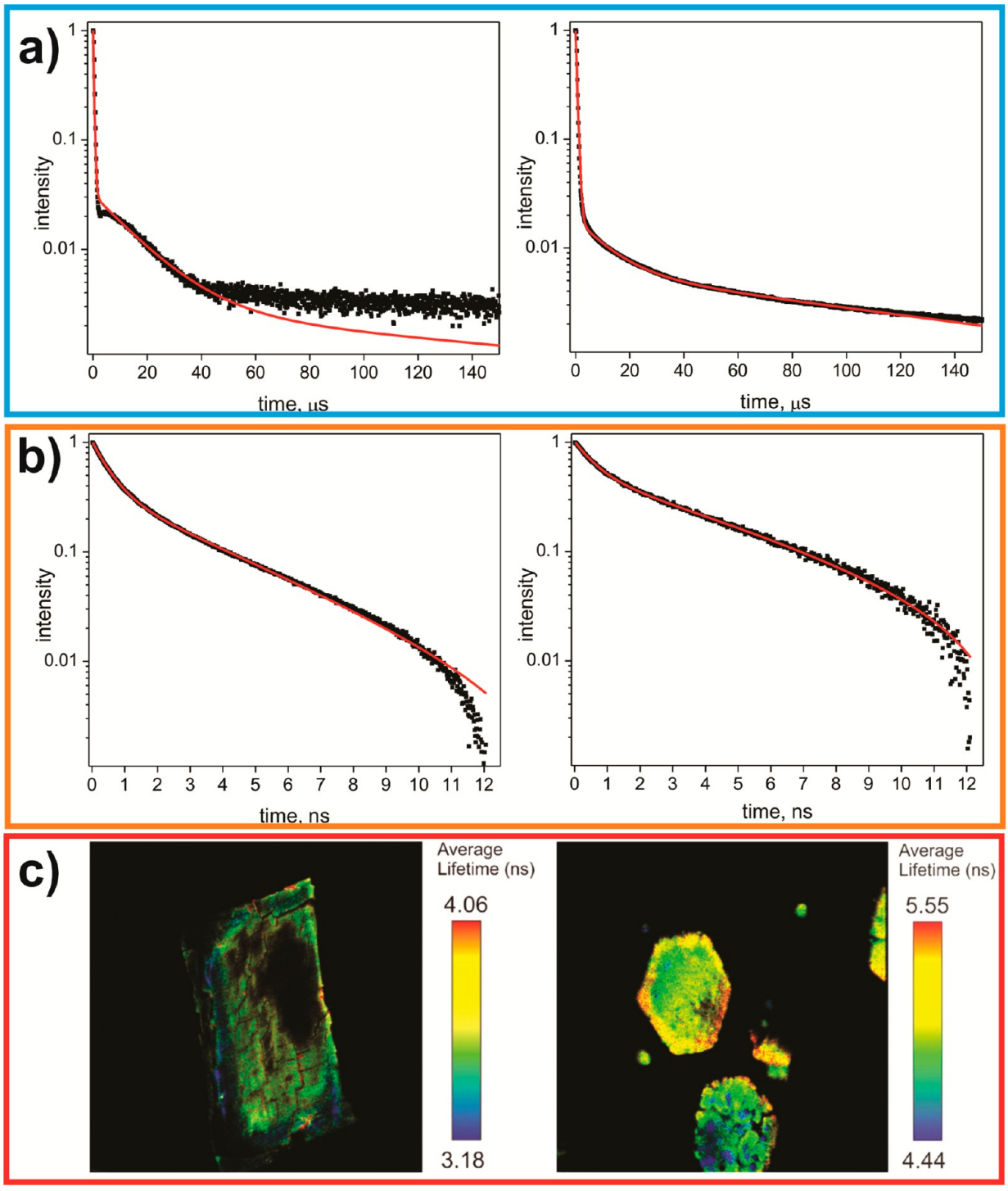

Figure 7. Normalized time-resolved PL decay traces for **1** (*left*) and **2** (*right*): microsecond (*a*) and nanosecond (*b*) time scales. All measurements were performed at room temperature. Solid lines show the fits to a sum of the exponential decay functions. Fluorescence-lifetime imaging microscopy (FLIM) micrographs (*c*), showing lifetime distributions for **1** (*left*) and **2** (*right*).

peak can be explained by (1) inhomogeneous distribution of surface coverage by selenophenolate ligands in any given nanocluster and by (2) existence of multiple conformational isomers for a given nanocluster. The latter explanation is supported by the observed lower line width for the emission spectrum obtained at $T = 77$ K, in agreement with decreasing of rotational flexibility of ligands in a frozen solution/glass. The temperature effect (rather than different nature of absorption or emission) also explains the red shift observed for both excitation and emission bands of **1**.

An assignment of the broad emission band of smaller CdSe nanoclusters as trapped emission was supported by time-resolved PL measurements, which showed nonexponential emission decay (distributed kinetics) on the microsecond time scale.[46,79] Calculated mean decay time τ (in Nujol suspension at $T = 10$ K; data approximation using stretched exponential function $\exp[-(t/\tau)^{\beta}]$) was found to decrease from 10.0 to

DOI: 10.1021/jacs.6b10490
J. Am. Chem. Soc. 2017, 139, 1129−1144

0.78 μs with nanocluster size increase from $(Pr_4N)_2[Cd_4(SePh)_6Cl_4]$ to $[Cd_{32}Se_{14}(SePh)_{36}(PPh_3)_4]$, respectively.[46] Significantly longer τ values were found at T = 20 K for the nanoclusters with the same size and core composition but having thiophenolate vs selenophenolate ligands, which provides an additional argument in favor of the involvement of surface phenylchalcogenolate ligands in the PL mechanism.[78] Time-resolved PL measurements for **1** at room temperature in micro- and millisecond time scales ($1.2\cdot10^{-7}$–$1.5\cdot10^{-3}$ s interval) show that the decay process is very complex and can be roughly fit as a sum of several exponential decay functions (Figure 7*a*, *left*). Most of the emission decays with τ_1 = 0.33 μs (and overall data were approximated as third-order exponential decay $\sum_{n=1}^{3} A_n\exp(-t/\tau_n)$. This value of τ for **1** (i.e., $[Cd_{54}Se_{32}(SePh)_{48}(dmf)_4]^{4-}$) is smaller than previously published 0.78 μs for $[Cd_{32}Se_{14}(SePh)_{36}(PPh_3)_4]$ and fits the trend of τ decrease with tetrahedral CdSe nanocluster size increase.[46] The key difference with previously reported smaller CdSe frameworks consists in the existence of other decay components with much longer life times (i.e., τ_2 = 15.6 and τ_3 = 190 μs). To check if any faster (than $\sim1\cdot10^{-7}$ s) processes can be revealed as well, additional time-resolved PL measurements are performed for **1** in the nanosecond time scale (Figure 7*b*, *left*). Fluorescence decay measurements, along with fluorescence-lifetime imaging microscopy (Figure 7*c*, *left*), show that in this time scale major emission intensity decay corresponds to τ = 3.6 ns. In general, the decay for **1** over the entire time scale is found to be multiexponential, with at least 2–3 components of lifetime in each time window. Such a broad range of lifetimes was observed previously for cadmium chalcogenide systems at low temperatures (for example, see ref 80) and discussed in terms of simultaneous radiative and nonradiative transitions between deeply trapped charge carriers, occurring with participation of various vibrational modes (multiphonon relaxation). Nonradiative relaxation for semiconductor nanoparticles and nanoclusters may include different processes that contribute to complex decay kinetics (e.g., Auger recombination, Förster resonance energy transfer, thermal escape and ligand-induced charge transfer);[81−84] the large number of possible relaxation pathways complicates the analysis. Overall, long-lived components in the time-resolved PL decay traces for **1** are consistent with the trapped emission associated with forbidden states involving the selenophenolate $PhSe^-$ surface ligands, although the possibility of radiative recombination via other defect states cannot be excluded.

The room-temperature emission of **1**, not observed for smaller members of capped supertetrahedral cluster family,[46] can be considered from the point of view of composition evolution upon the cluster size increase in the homologues series (Table 1). As nonradiative relaxation in $[Cd_{17}Se_4(SePh)_{24}L_4]^{2+}$ and $[Cd_{32}Se_{14}(SePh)_{36}L_4]$ (L = PPh_2Pr and PPh_3, respectively) at room temperature was proposed to occur through vibrating modes of the bridging selenophenolate ligands (μ-$SePh^-$) at the nanocluster edges,[46,79] the increase of the cluster size while progressing toward $[Cd_{54}Se_{32}(SePh)_{48}L_4]^{4-}$ may diminish this effect due to decreasing the fraction of surface sites. Thus, change in nanoclusters composition in capped tetrahedral cluster family can be followed in the case of different Se sites (Table 1): surface-to-core ratio (μ-$SePh^-/\mu_4$-Se^{2-} sites) decreases from 6:1 to 2.4:1 in Cd17 and Cd54,[85] respectively. For the latter cluster, relaxation from the excited state through selenophenolate ligands vibrations may become less influential, and emission (slow radiative transitions involving trapped states) is observed. This hypothesis is consistent with previous observations that the temperature at which the emission of nanoclusters reduces to the background level increases progressively with increasing nanocluster size from $(Pr_4N)_2[Cd_4(SePh)_6Cl_4]$ through $[Cd_{10}Se_4(SePh)_{12}(PPr_3)_4]$ and $[Cd_{17}Se_4(SePh)_{24}(PPh_2Pr)_4]^{2+}$ to $[Cd_{32}Se_{14}(SePh)_{36}(PPh_3)_4]$.[46] Then, larger members of capped supertetrahedral cluster family possess surface μ_3-Se^{2-} sites. Surface ligand-to-ligandless ratio (μ-$SePh^-/\mu_3$-Se^{2-} sites) decreases from 9:1 to 4:1 in Cd32 and Cd54,[85] respectively. Such differences in surface composition may also contribute to emission properties of **1**. Moreover, it was observed experimentally and confirmed by theoretical calculations at DFT and TDDFT levels for tetrahedral CdE nanoclusters belonging to different families, that the influence of ligands on the photophysical properties becomes less pronounced with increasing cluster sizes (see, for example, ref 86).

Examination of the optical properties of **1** allowed to reveal both similarities and differences from the trends for structurally related smaller cadmium chalcogenide nanoclusters reported previously. Thus, comparison of UV–vis absorption, diffuse reflectance and PLE spectra of **1** with those of smaller members of capped supertetrahedral cluster family shows, that low-energy peak positions are consistent with systematical shift due to quantum confinement effect. This can be illustrated by the red shift of the low-energy excitonic peak maximum in UV–vis spectra from 341 and 373 to 410 nm with nanoclusters size increase from $[Cd_{17}Se_4(SePh)_{28}]^{2-}$ and $[Cd_{32}Se_{14}(SePh)_{36}(PPh_3)_4]$[45,46] to **1** (i.e., $[Cd_{54}Se_{32}(SePh)_{48}(dmf)_4]^{4-}$), respectively. Unlike smaller family members, room temperature PL spectra of **1** in DMF solutions, as well as its room temperature solid state PL spectra, show the presence of distinct emission with maxima at 545 and 582 nm, respectively. Based on the considerable red shift from the excitation maximum, the broad line width and long-lived components in multiexponential emission decay, the observed emission was attributed to deep trap states related to surface selenophenolate $PhSe^-$ ligands. CdSe nanoparticles (average diameter ~4 nm) with phenylchalcogenolate ligands were also previously reported to show broad long-lived trapped emission at 77 K while no emission at room temperature; in the latter case relaxation was assigned to a combination of hole transfer to the ligand (more efficient at higher temperature and for the ligands in the row PhS^- < $PhSe^-$ < $PhTe^-$) and of phonon-assisted nonradiative decay pathways.[87] In contrast, room temperature trapped emission (broad band at 604 nm) was reported for much smaller CdSe nanoparticles with thiophenolate ligands.[88] Generally, a complex relationship among nanocluster/nanoparticle size, shape, surface structure and relaxation pathways in the system may exist; the surface science

Table 1. Composition of the Members of Capped Tetrahedral Nanocluster Series

Cluster formula[a]	Number of μ_4-Se^{2-} sites (tetrahedral)	Number of μ_3-Se^{2-} sites (tricoordinated pyramidal)	Number of edge μ-$SePh^-$ sites (bridging)
$[Cd_{17}Se_4(SePh)_{24}L_4]^{2+}$	4	0	24
$[Cd_{32}Se_{14}(SePh)_{36}L_4]$	10	4	36
$[Cd_{54}Se_{32}(SePh)_{48}L_4]^{4-}$	20	12	48

[a]L represents a neutral ligand, such as H_2O or *dmf*.

DOI: 10.1021/jacs.6b10490
J. Am. Chem. Soc. 2017, 139, 1129–1144

of nanoscale objects represents the area of active scientific research where many phenomena are still far from being fully understood.[89] Further investigation will be necessary for better understanding of observed unprecedented room temperature emission of **1** and the exact mechanism for "unquenching" in the presence of $PhSe^-$ surface ligands.

2. Going Beyond Discrete Nanoclusters: Three-Dimensional Crystalline CdSe Network. It was shown previously that Br^- ions in reaction solutions influences the thermally induced condensation of the sulfur complex $(Me_4N)_2[Cd(SPh)_4]$ in DMF, resulting in the formation of larger (in comparison to additive-free synthesis) monodisperse CdS nanoclusters, arranged into cubic superlattices.[60] In a similar fashion, the addition of CTAB to solutions of $(Me_4N)_2[Cd(SePh)_4]$ was found to have a marked effect on the size and arrangement of the CdSe particles generated under solvothermal conditions.

Solvothermal treatment of $(Me_4N)_2[Cd(SePh)_4]$ in the presence of CTAB yields a solid product, which comprises two distinct materials: relatively large, brick-red hexagonal prisms (**2**), which sediment readily from the mixture, and fine, shapeless, orange aggregates, which remain suspended in the mother liquor or pure DMF unless centrifuged. Material **2** was separated, dried and examined more closely.

2.1. Structure and Morphology. Despite the fact that the hexagonal prisms demonstrate some characteristics of a single crystal (e.g., they are well-faceted and show single crystalline behavior in polarized light), multiple attempts of single-crystal X-ray characterization for fresh **2** were not successful: the samples display diffuse scattering streaks rather than clearly discernible Bragg reflections. Although a regular pattern can be observed from the X-ray scattering (SI *Figure S8*), the data are insufficient to derive additional information on the structure of material **2**.

Optical microscopy and subsequent SEM examination of dried **2** revealed that all well faceted hexagonal prisms have similar proportions. According to SEM (Figure 8), the size of

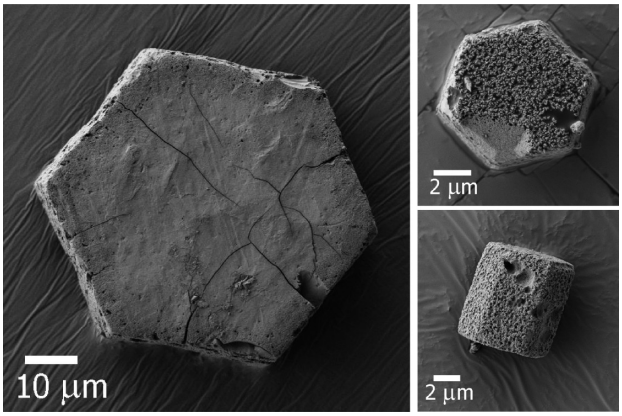

Figure 8. SEM images of representative hexagonal prisms in **2**. Top (*left* and *top right*) and side (*bottom right*) views are shown.

majority of the prisms is approximately 50 μm (distance between opposite corners of the hexagonal base) and about the same in height. Much smaller (<10 μm) and larger (>70 μm) prisms are also seen but relatively rare. High resolution SEM of selected hexagonal prisms allows more details to be observed: although the surface of some prisms is relatively smooth (SI *Figure S9*, *left*), in other prisms it is partially or entirely roughened (SI *Figure S9*, *center* and *right*). Larger defects, such as cracks and cavities, are also seen. Cracks are observed exclusively on the hexagonal bases; smaller hexagonal prisms appear to contain fewer defects. Specific localization of the continuous defects may suggest that the nature of cracking in **2** (presumably, shrinkage cracking, see below) is different from that suggested for material **1**.

In the low-angle PXRD patterns for dried **2**, a sharp but not very intense reflection is found at 2θ 2.68°, and a weak, broad one is observed at 5.38° (i.e., at double the angle of the main diffraction peak) (SI *Figure S10*). Low-angle PXRD reflections provide evidence of long-range order present in hexagonal prisms. The lowest angle reflection is shifted substantially toward the lower values due to a larger unit cell in comparison to that of dried **1**. Thus, the calculated interplanar spacing d for **2** is 3.83 nm, whereas for **1** it is only 2.05 nm. In the wide-angle region of the PXRD patterns for **2**, reflections are narrower in comparison to those in the patterns for **1**. It is interesting that some features characteristic of the hexagonal CdSe structure can be discerned (e.g., 100 and 101 reflections around 2θ 30°). However, no sign of the 103 reflection for the hexagonal CdSe is observed, which argues in favor of the cubic CdSe structure. Substantial breadth of peaks in the wide-angle region complicates the analysis of the internal crystalline structure in this case, as it was described previously for CdSe nanoparticles (see, for instance, ref 90) and many other nanodimensional objects.[91] Calculations of the mean size of the crystalline domains using the Scherrer equation for the dried material **2** give a value of 2.26 nm, which is larger than 1.55 nm in the case of **1**.

2.2. Composition. Raman spectra of **2** (SI *Figure S1*) contain very similar bands as those observed for **1**, showing the general similarity in composition of these two materials. For instance, bands at 197 cm^{-1} due to interior Cd−Se bonds, 666 cm^{-1} due to surface Se−C bonds and 3052 cm^{-1} due to aromatic C−H bonds can be assigned, confirming the supposition that **2** represents crystalline CdSe with $PhSe^-$ ligands on its surface. The difference between **1** and **2** consists in the relative intensities of the Raman bands. To facilitate their comparison, the Raman spectra of **1** and **2** were normalized to the intensity of the band at ∼200 cm^{-1} (assigned as stretching vibrations of interior Cd−Se bonds). Such normalization allows for evaluation of surface/interior group ratio; it can be concluded that the relative intensity of any bands related with organic ligands is smaller for **2** in comparison with **1**. A representative example is the band at 666 cm^{-1} due to surface Se−C bonds: a decrease in intensity of this band from **1** to **2** is in agreement with the decrease in the overall selenophenolate to selenide ($PhSe^-/Se^{2-}$) ratio. Because there are no aliphatic C−H Raman bands of high intensity present in the spectra of **2** (i.e., bands at 2992 and 2935 cm^{-1} are very weak), it is more likely that neither CTAB nor any possible products of its decomposition are "ensnared" inside the prisms or on their surface. Similarly, there is hardly any residual solvent (DMF) in **2** present. Overall, it can be suggested that the organic component in hexagonal prisms is mainly $PhSe^-$.

Site-specific EDX spectroscopy analysis of hexagonal prisms in **2** confirms the composition $[Cd_xSe_y(SePh)_z]$; the Cd/Se atomic ratio was found to be 1.06:1, which is a reasonable value for continuous CdSe network.[92] No Br was found in a detectable amount in **2** by EDX analysis, which suggests that the halide may facilitate fusion of lower-nuclearity cadmium selenophenolate intermediates leading to growth of larger

DOI: 10.1021/jacs.6b10490
J. Am. Chem. Soc. 2017, 139, 1129−1144

constituents (similar to what was previously concluded for related CdS systems),[60] but not being present in the final product. Halogen-containing additives were also recently found to influence both the kinetics and thermodynamics of CdSe nanoparticles growth, presumably via unequal participation of Hal^- in dynamic absorption/desorption processes on different crystalline facets; in this case, halide ligands where then clearly detected in purified samples.[93] An absence of Hal^- in **2** (and in **1** as well) is a significant result because halide ligands are known to influence emission of cadmium chalcogenide nanoclusters and nanoparticles.[94−96]

2.3. Optical Properties. Unlike **1**, which is soluble both in DMF and acetonitrile, even prolonged stirring of **2** in DMF does not result in solutions with any detectable UV−vis absorption bands. The UV−vis diffuse reflectance spectra of solid **2** (Figure 9) are essentially structureless with only very

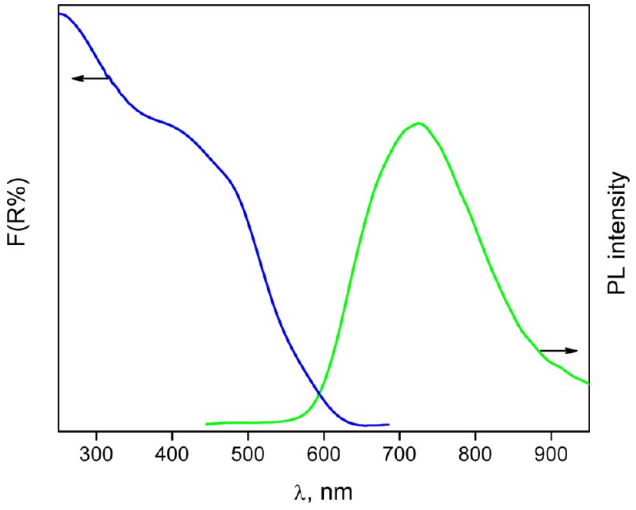

Figure 9. UV−vis diffuse reflection spectrum of solid **2** (processed using the Kubelka−Munk function and normalized); room temperature solid state PL spectrum of **2** (normalized). For solid state PL spectrum, the excitation wavelength was 405 nm.

broad bands at ~475 and 405 nm. An onset of the absorption is more gently sloping and shifted toward a longer wavelength in comparison to the diffuse reflectance spectra of **1**. Both red shift of the absorption onset and the negligibly small solubility of **2** in comparison with **1** is consistent with the larger size of constituent elements in **2**, also derived from PXRD patterns.

The hexagonal prisms of dried **2** show clearly visible red luminescence at room temperature; on the confocal fluorescence microscopy images, bright emission is observed from all hexagonal prisms regardless of their size (Figure 10, *top*). The apparent uneven brightness of emission is assumed to originate mainly from differing orientations of the hexagonal prisms (lying flat on a base, or flat on a side, or tilted at some angle, see Figure 10, *top*). Note that the hexagonal prisms lying flat on a side look as rectangles in this projection. For a single prism, nearly homogeneous emission is observed from any spot on each side (e.g., the hexagonal base, Figure 10, *bottom*).

The emission spectra of dried **2** show a distinct broad (fwhm 185 nm) band at 725 nm (Figure 9), attributed to trapped emission. A remarkable red-shift in comparison with solid state emission maximum for **1** (observed at 582 nm) may suggest the difference in surface chemistry between these two materials (which is consistent with the difference in their organic ligand

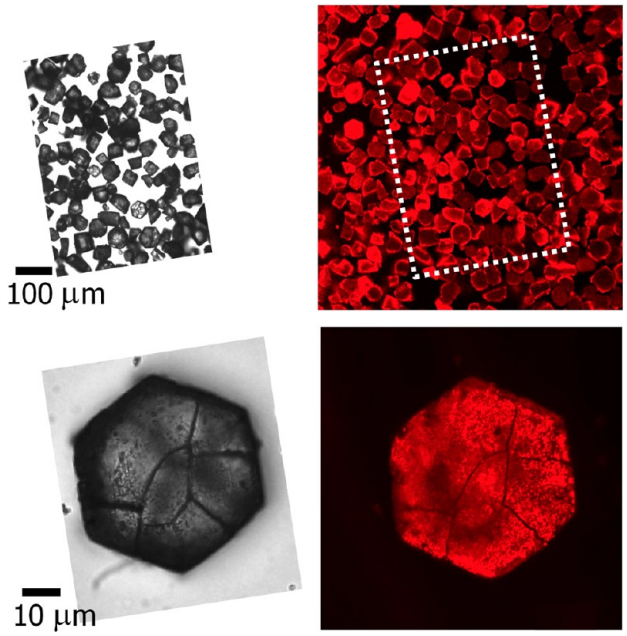

Figure 10. Transmission optical (*left*) and confocal fluorescent microscopy (*right*) images of hexagonal prisms of **2**: multiple (*top*) and single (*bottom*). The confocal fluorescence microscopy images are pseudocolored red.

shells, observed by Raman spectroscopy). The difference in optical properties may also be related to the fact that the structure of materials **1** and **2** is remarkably different (as revealed by powder X-ray diffraction measurements).

Time-resolved PL measurements show that decay traces for **2** (Figures 7*a*−7*b*, *right*) are substantially different from those for **1** in both nano-, micro- and millisecond time scales. Thus, obtained data for the long-living processes (Figure 7*a*, *right*) fit a third-order exponential decay with τ_1, τ_2 and τ_3 being 0.54, 12.0 and 132 μs, respectively. In the nanosecond time scale (Figure 7*b*, *right*), a major emission intensity decay for **2** corresponds to τ = 5.0 ns, whereas the lifetime distribution (Figure 7*c*, *right*) is similar to observed for **1**. The complexity of the decay processes does not allow for the strict attribution of the relaxation pathways for **2**, as the set of observations can be explained by different scenarios. For instance, slower room temperature decay on the nanosecond scale for **2** in comparison with **1** may be related with the difference in fast phonon-assisted nonradiative decay[87] due to a different sample structure (presumably, continuous CdSe network for **2** vs superlattice of noncovalently bonded nanoclusters for **1**). Similar rates of emission decay for **2** and **1** on the microsecond time scale may refer to radiative and nonradiative transitions due to trapped states related with the same surface ligands for both samples (i.e., $PhSe^-$; lifetimes > 100 μm).[87] Then, considerably faster decay for **2** in comparison with **1** on a millisecond time scale may be related to a smaller $PhSe^-/Se^{2-}$ ratio in the case of **2**.

2.4. Internal Organization. Knowing the internal organization within the hexagonal prisms was assumed to be the key for better understanding the optical properties of material **2**. Because very similar composition and optical properties were observed for smaller and larger hexagonal prisms found in **2**, the difference in sample size seems not to be induced by the difference in nature of the material. As fewer defects were usually found with the smaller prisms, it makes them more

DOI: 10.1021/jacs.6b10490
J. Am. Chem. Soc. 2017, 139, 1129−1144

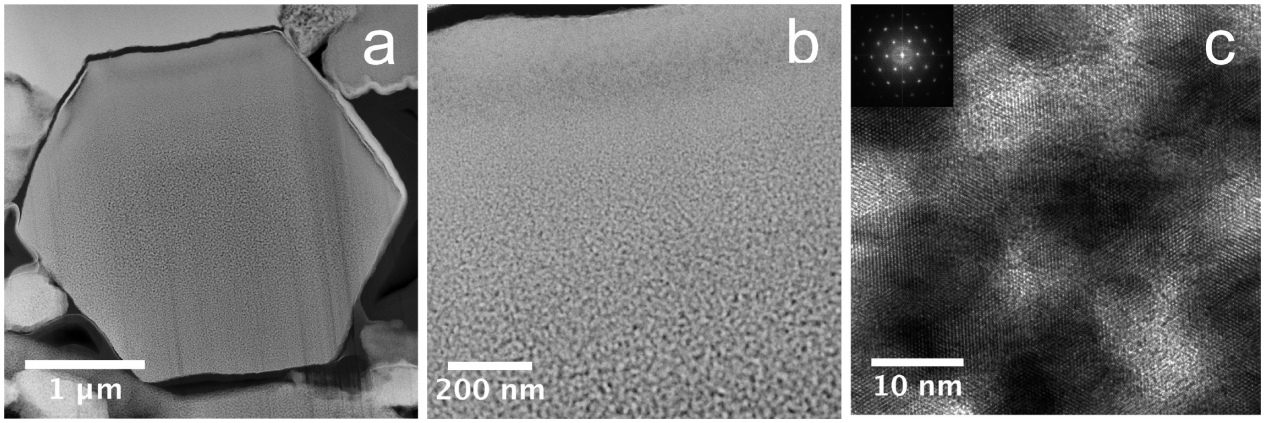

Figure 11. STEM images of thin slice through hexagonal prism **2**: general view (*a*); gradient from face to center shown from top to bottom (*b*). TEM image of central part of hexagonal prism (*c*). Inset: Fourier transform of TEM image showing reflections due to crystalline CdSe structure.

convenient for sample preparation for electron microscopy examination. A relatively small (~3.2 μm between opposite corners of hexagonal base) hexagonal prism was localized in **2** under a SEM (SI *Figure S11, left*) and used for sample preparation by FIB milling. Note that the sample of **2** selected was not separated from the accompanying byproduct, and thus also contains some shapeless aggregates. A thin slice was obtained perpendicular to the main axis of the hexagonal prism (SI *Figure S11, right*). An assumption is made that such a slice is representative of the elements throughout the internal structure of the hexagonal prism.

STEM and TEM examination of the as-prepared slice reveal that the inner part of the hexagonal prism is heterogeneous (Figure 11a). Due to the intergrowth nature of the internal structure, specific particle sizes are not discernible for the visible constituent elements, which appear as brighter regions on STEM and as darker regions on TEM images (Figures 11*b* and 11*c*, respectively). No obvious pattern can be found for the constituent elements; with electron microscopy imaging looking at a two-dimensional projection, the exact internal structure of the prism **2** in three dimensions can not be unraveled. Nevertheless, it is intriguing that clear gradients in the size of the constituent elements can be seen from the lateral face to the center of the prism (Figure 11*b*), whereas in the localized areas (e.g., central part only or small fragment closer to the edge only) the constituent elements appear to be approximately the same in size. The obtained images can be interpreted in two alternative ways: (1) the prism is composed of individual CdSe nanoparticles of different size (a size gradient from smaller particles at the surface to larger ones at the center); or (2) the prism represents continuous three-dimensional network of solid CdSe material (an inorganic phase thickness gradient changing on the nano scale from thinner walls at the surface to thicker ones at the center). In both cases, CdSe domains alternate with other domains that are more transparent to the electron beam (most likely, organics). The key difference between these two interpretations is whether CdSe forms a discrete (nanoparticles) or continuous (interconnected walls) phase.

The hexagonal prism is crystalline with visible rows of atoms seen at the higher resolution TEM images (Figure 11*c*). Fourier transform of the TEM images of the central part of the hexagonal prism shows individual spots due to a coherent crystalline CdSe structure throughout the (continuous) examined areas (Figure 11*c*, *inset*); similar results were also obtained while analyzing TEM images of other parts of the prism. The electron diffraction patterns obtained from most of the prism area exhibit well-defined single-crystal-like reflections (Figure 12), as if the hexagonal prism would be one single

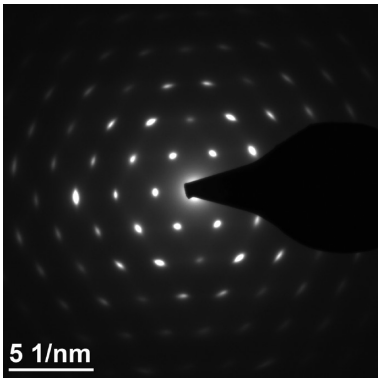

Figure 12. SAED of the thin slice of the hexagonal prism **2**, characterizing the CdSe crystalline lattice of the inorganic phase.

crystal with a pore-like structure. Additional bright-field and dark-field TEM images are in agreement with single-crystal-like behavior of **2** (SI *Figure S12*), as uniform crystalline lattice orientation can be observed through the whole slice of the hexagonal prism.

A perfect alignment of the CdSe crystalline lattice throughout continuous domains in apparently heterogeneous formation could only be possible when there is a strong interaction (connection) between constituent components. Thus, different degrees of partial alignment of an intramolecular crystalline lattice are usually observed in superlattices of individual nanoclusters, as only relatively weak (e.g., van der Waals) cluster−cluster interactions hold the order in secondary structure. In the wide-angle electron diffraction patterns of such superlattices, segmented rings are typically observed. Dried **1** and related superlattices of larger CdS nanoclusters[60,97] represent such a case. Unlike in the case of nanocluster superlattice, individual reflections are observed in the wide-angle electron diffraction patterns for **2**. Hence, both TEM and SEAD provide evidence in favor of a three-dimensional crystalline CdSe network in **2**, interspaced with a second phase (most probably, organic matter). N_2 adsorption analysis revealed only a very small accessible BET surface area for **2**

DOI: 10.1021/jacs.6b10490
J. Am. Chem. Soc. 2017, 139, 1129−1144

(<1 m^2/g). A superstructure represented with a single crystal having complex morphology was reported by Nogami et al.,[98,99] with crystalline Pt primary particles (~5 nm in size) assembled into porous secondary structures in the shape of cubes (20−80 nm in length) in such a way that they have a coherent crystalline structure, as confirmed by TEM and SAED.

The presence of a three-dimensional crystalline CdSe network provides background for explaining the optical properties of material **2**. Thus, the substantial red shift of solid state emission maximum in comparison with **1** (for which the same origin of radiative transitions, i.e., trapped emission related with surface $PhSe^-$ ligands, can be suggested) can be rationalized taking into account different surface curvature and larger surface-to-volume ratio in **2** vs **1**. The larger size of constituent elements in **2** vs **1** would not likely cause such a red shift, as trapped emission was previously reported to be virtually size-independent.[46] The difference in structures for **2** and **1** will also qualitatively explain the difference in emission decay of these materials, as a continuous network would have, for instance, different parameters for phonon-assisted non-radiative decay vs superlattice of individual nanoclusters. The difference in positions of the medium-strong band in Raman spectra, assigned to the stretching vibrations of interior Cd−Se bonds (197 and 201 cm^{-1} for **2** and **1**, respectively) argues in favor of such an interpretation.

A three-dimensional crystalline CdSe network in **2** could potentially be disordered or possess secondary (with respect to crystalline lattice) order. In the latter case, such ordered secondary structure can be referred to as a mesostructure, i.e., material with the properties intermediate between amorphous and crystalline solids and comprising constituent elements with sizes between 2 and 50 nm.[100−102] Despite the apparent lack of the regular pattern seen on electron microscopy images, the right geometrical shape of the hexagonal prisms is most probably related to intricate internal periodicity. The presence of reflections in the low-angle region of the PXRD patterns for **2** also suggests that certain long-range order exists. Additional examination (e.g., electron tomography) may help to gain more information about the internal structure of the hexagonal prisms.

2.5. Formation Mechanism. Vapor phase, solution-based and solid-state preparation of crystalline micro- and nanoparticles possessing a shape of hexagonal platelets or hexagonal prisms was reported previously for many metal chalcogenide systems, including d-block (e.g., Ni, Cu or Cd)[103−109] and main group metals (e.g., In, Sn or Sb)[110−115] as well as multinary systems (e.g., Bi−Sb and Yb−Sb).[116,117] In the majority of cases, the growth of anisotropic particles is related with the inherent anisotropy of a crystal structure (e.g., the shape is dictated by the trigonal unit cell) or different reactivity of crystal facets (including the facet-specific adsorption of ligands), while some exceptions are also known. For instance, STEM and SAED examination of solvothermally prepared single crystalline Sb_2Te_3 hexagonal nanoplatelets and several intermediates (isolated upon process quenching at different reaction times) revealed apparently amorphous intermediate possessing hexagonal shape.[118] Micrometer-sized particles in the shape of hexagonal platelets representing a superlattice of nearly monodisperse CdSe nanoparticles were also reported.[119] To the best of our knowledge, no CdSe hexagonal prisms having heterogeneous (porous) single-crystal structure have been reported.

A supposition can be made that the three-dimensional crystalline CdSe network in **2** is created by fusion of preformed crystalline CdSe nanoparticles. Results of analyses (see SI *Appendix A*) of the orange material lacking a distinctive shape, present among the products of solvothermal synthesis along with red hexagonal prisms **2**, support this. The orange material is found to be nonregular aggregates of polydisperse CdSe nanoparticles (larger than nanoclusters in **1**) with stabilizing organic shell of primarily $PhSe^-$ ligands.

Particle-mediated crystallization via oriented attachment mechanism was previously discussed as a possible (non-classical) pathway of crystalline materials formation.[18−22] This mechanism assumes irreversible self-assembly of nanometer-sized crystalline building blocks into continuous superstructure by alignment and fusion of appropriate crystal facets. An atomic matching of the facets in a process of such connection leads to the formation of iso-oriented crystalline lattice in continuous homo- or heterogeneous material.[120,121] In the first case the process results in conventional crystals, while in the second it results in crystalline mesostructures, such as porous crystals and sponge crystals.[122] Oriented attachment is different from nanocluster self-assembly into an ordered superlattice in the strength of the cohesive forces, which are covalent cluster−cluster bonding in the first case and noncovalent interactions (e.g., electrostatic or van der Waals) in the second case. In turn, oriented attachment is different from random aggregation (coalescence) by the presence of strong alignment preference for crystalline nanoparticles fusion.[123] A few examples of three-dimensional crystalline mesostructures achieved by oriented attachment for group 12-16 compounds include self-assembly of ~5 nm ZnO crystalline nanoparticles into highly uniform ZnO mesoporous ellipsoids with length and width up to 190 and 111 nm, respectively.[124]

Similar to these, the formation of hexagonal prisms **2** may occur through several consecutive steps: (1) growth of crystalline faceted CdSe nanoparticles, stabilized by $PhSe^-$ ligands; (2) assembly and alignment of primary CdSe nanoparticles into metastable formation (kept together by relatively weak forces, like van der Waals) with iso-oriented crystalline lattices of individual building blocks; (3) docking and fusion of oriented primary CdSe nanoparticles into continuous solid CdSe network with remnants of original organic stabilizers (i.e., $PhSe^-$ ligands). In other words, upon the oriented attachment the individual nanoparticles build up walls of continuous solid CdSe network (seen as brighter regions on STEM and as darker regions on TEM images, Figure 11). The resulting three-dimensional network retains the size-related properties of its nanodimensional constituents, as thickness of the CdSe walls is related to the dimensions of primary CdSe nanoparticles. The formation of the three-dimensional CdSe network by fusion of relatively large primary nanoparticles is consistent with relatively low organic ligand content for **2** in comparison with **1**, revealed by Raman spectroscopy. From these analyses, it also follows that the organic component in the heterogeneous structure **2** is mainly surface $PhSe^-$ ligands of the CdSe network. According to proposed scheme, the cracking of hexagonal prisms **2** is rather related with network shrinkage accompanying formation of mesoporous nanomaterials[125] than removal of crystallization solvent from noncovalently bonded nanocluster superlattice, as it is proposed for **1**.

DOI: 10.1021/jacs.6b10490
J. Am. Chem. Soc. 2017, 139, 1129−1144

CONCLUSIONS

Two distinct superstructures of nanoscopic CdSe were prepared using solvothermal conversion of the same cadmium selenophenolate precursor $(Me_4N)_2[Cd(SePh)_4]$. The first is a superlattice of monodisperse CdSe nanoclusters and the second a unique porous CdSe crystal. Nanoclusters were crystallized as cubic crystals (≤0.5 mm in size) after solvothermal treatment at 200 °C in DMF. The molecular formula $(Me_4N)_4[Cd_{54}Se_{32}(SePh)_{48}(dmf)_4]$ was proposed for this material based on single-crystal X-ray diffraction and a set of auxiliary analyses (including Raman spectroscopy and TGA). Some peculiarities of this large nanocluster superlattice (including triggered-by-autoclave-opening crystallization and superlattice rearrangement upon drying) were observed. UV−vis absorption spectra of mother liquor before and after crystallization of $[Cd_{54}Se_{32}(SePh)_{48}(dmf)_4]^{4-}$ show that these nanoclusters are the main product of precursor conversion. UV−vis absorption and PLE spectra of nanoclusters $[Cd_{54}Se_{32}(SePh)_{48}(dmf)_4]^{4-}$, comparing with those of smaller members of the same capped supertetrahedral cluster family, are consistent with the previously established trends, as they show systematical shift of the low-energy peak positions due to quantum confinement effect and composition change. In contrast to this, results of PL spectra of nanoclusters $[Cd_{54}Se_{32}(SePh)_{48}(dmf)_4]^{4-}$ are rather unexpected, as distinct room temperature emission is observed both in solutions and in solid state. Detailed examination (including time-resolved PL measurements) points to the conclusion that the emission is associated with forbidden states involving the selenophenolate $PhSe^-$ surface ligands (trapped emission), which is unusual to be detected at room temperature. Additional experiments will help to elucidate the nature for observed "unquenching" in the presence of $PhSe^-$ surface ligands in nanoclusters $[Cd_{54}Se_{32}(SePh)_{48}(dmf)_4]^{4-}$.

A second CdSe superstructure was isolated as red hexagonal prisms (≤70 μm in size) among the products of the solvothermal treatment under similar conditions but with addition of CTAB. The presence of three-dimensional CdSe network having a coherent crystalline structure inside hexagonal prisms was concluded based on powder X-ray diffraction, SAED and electron microscopy imaging. As it was revealed by Raman spectroscopy, an organic component of in the network is represented with $PhSe^-$ ligands on surface. Self-assembly via oriented attachment of crystalline nanoparticles is discussed as the most probable mechanism of formation of porous CdSe crystal hexagonal prisms. Neither Br^- nor any long-tail alkylammonium residues were detected in the final product. The role of Br^- in the superstructure growth may lie in facilitating the fusion of lower-nuclearity intermediates during the solvothermal process with formation of primary nanoparticles as well as in subsequent fusion of oriented nanoparticles into continuous CdSe network. Red hexagonal prisms also exhibit distinct trapped emission at room temperature; maximum in solid state PL spectrum is remarkably red-shifted in comparison with that for $[Cd_{54}Se_{32}(SePh)_{48}(dmf)_4]^{4-}$ nanoclusters superlattice. The difference in optical properties of two prepared superstructures is attributed to their unlike morphology.

The results give an insight into the solvothermal preparation of nanoscopic CdSe materials with intriguing structure and unprecedented optical properties. This information may potentially help in tuning properties and rationally designing architecture of functional materials targeting application in electronics and optoelectronics.

EXPERIMENTAL SECTION

All synthetic and handling procedures were carried out under an atmosphere of high-purity dried nitrogen using standard double manifold Schlenk line techniques and a MBraun Labmaster 130 glovebox.

Syntheses of CdSe nanoscopic superstructures **1** and **2** were performed in a sealed reactor (autoclave) at controlled temperature and increased pressure using DMF (solvothermal conditions). The reagents were mixed and sealed in autoclaves under inert atmosphere in the glovebox; heating the sealed autoclaves in an oven was performed under ambient atmosphere, whereas autoclave opening and product isolation were performed again under inert atmosphere.

Preparation of 1. The product **1** can be achieved using a range of selected reaction parameters (such as precursor concentration, volume of solution, duration and temperature of solvothermal treatment). The typical synthetic procedure was as follows: $(Me_4N)_2[Cd(SePh)_4]$ (1.062 g; 1.20 mmol) was combined with DMF (5 mL) in a 30 mL glass bottle and mixed with magnetic stirrer for 15−30 min resulting in a colorless solution over a small amount of undissolved precursor. The bottle was sealed in a stainless steel autoclave and placed into a preheat oven at 200 °C for 24 h. The oven was then opened, and the sealed autoclave was allowed to cool naturally to ambient temperature over ∼2 h. The autoclave was opened and the reaction solution (turbid orange-yellow liquid) was immediately filtered (0.22 μm, PTFE 100/pk membrane, Dikma Technologies Inc.) and left undisturbed at room temperature. Yellow cubic crystals of **1** rapidly grow (mainly over the period 2−24 h; after several days or even a few weeks, more identical crystals may appear). The crystals with some mother liquor were used for single-crystal and powder X-ray diffraction ("fresh **1**"); for other analyses, material was isolated and dried ("dry **1**") as follows. The crystals were collected by centrifugation at 4000 rpm for 5 min, quickly washed with small portion of acetonitrile and several times with copious amount of methanol, then dried under vacuum for 1−2 h. Mass yield ∼0.05 g.

Preparation of 2. The procedure for the preparation of **2** was generally similar to that used for **1** except particular modifications. Thus, solvothermal synthesis in this case was performed in Teflon bottles sealed with Teflon tape; attempts to reproduce synthesis in glass bottle resulted in a less morphologically sophisticated product. $(Me_4N)_2[Cd(SePh)_4]$ (1.51 g; 1.71 mmol) was combined with DMF (5 mL) and mixed with magnetic stirrer for 15−30 min resulting colorless solution over noticeable amount of undissolved precursor. CTAB (0.311 g; 0.85 mmol) was added and stirred for another 15−30 min producing white suspension. The bottle was sealed in a stainless steel autoclave and placed into preheat oven at 200 °C for 48 h. The oven was then opened, and the sealed autoclave was allowed to cool naturally to ambient temperature over ∼2 h. The autoclave was left undisturbed for another 48 h and then opened; very turbid orange liquid and brick-red heavy solid product (often attached to inside walls and bottom of Teflon bottle) were typically found. Brick-red solid (the main product) was separated from orange solid byproduct using multiple washing with DMF: the red fraction is insoluble in DMF and sediments quickly, whereas the orange fraction is slightly soluble in DMF and stays suspended unless centrifugated. Brick-red solid was washed well with MeOH and dried under vacuum for 1−2 h. Mass yield 0.03−0.06 g.

While the synthetic pathway toward **1** allows for considerable variation of selected reaction parameters (see SI *Supplementary Synthetic Details*), the preparation of **2** as well-faceted hexagonal prisms is much more demanding, requiring the optimized reaction conditions.

Elemental analysis (CHNS) was performed by Laboratoire d'Analyze Elémentaire de l'Université de Montréal (Quebec, Canada). The values of nitrogen found for **1** were less than the minimum detection limit (0.3%). Results are reported as an average of two measurements. Calcd for $Cd_{54}Se_{80}C_{316}H_{316}N_8O_4$

DOI: 10.1021/jacs.6b10490
J. Am. Chem. Soc. 2017, 139, 1129−1144

($(Me_4N)_4[Cd_{54}Se_{32}(SePh)_{48}(dmf)_4]$): C, 22.76; H, 1.91; N, 0.67%. Calcd for $Cd_{54}Se_{80}C_{324}H_{288}N_4O_4$ ($[Cd_{54}Se_{28}(SePh)_{52}(dmf)_4]$): C, 23.32; H, 1.74; N, 0.34%. Found for **1**: C, 23.67; H, 1.64; N, 0.28%

■ ASSOCIATED CONTENT

Supporting Information

The Supporting Information is available free of charge on the ACS Publications website at DOI: 10.1021/jacs.6b10490.

Crystallographic data for **1**, supplementary synthetic and characterization details; Raman spectra of **1** and **2**; mass spectra and thermogravimetric data for **1** along with interpretation; supplementary UV−vis absorption and PL/PLE spectra; supplementary SEM and TEM images; and supplementary PXRD patterns. Appendix A includes characterization of the material coexisting with **2**. (PDF)

CIF for **1** (CIF)

■ AUTHOR INFORMATION

Corresponding Authors

*(Y.H.) E-mail: yhuang@uwo.ca.

*(J.F.C.) E-mail: corrigan@uwo.ca.

ORCID

John F. Corrigan: 0000-0003-2530-5890

Author Contributions

All authors have given approval to the final version of the manuscript.

Funding

The authors thank the Natural Sciences and Engineering Research Council (Canada) Discovery Grants and Equipment Grants Programs (J.F.C. and Y.H.) and a Doctoral Postgraduate Scholarship (T.I.L.) for financial support. Y.H. acknowledges the support of the Canada Research Chairs Program. J.F.C. thanks the Centre for Functional Nanostructures (Karlsruhe Institute of Technology, Germany) for a Visiting Professorship. This work was partly carried out with the support of the Karlsruhe Nano Micro Facility (KNMF, www.kit.edu/knmf), a Helmholtz Research Infrastructure at Karlsruhe Institute of Technology (KIT, http://www.kit.edu/). The visit of T.I.L. to the KNMF, KIT, was supported by an ASPIRE award (Western).

Notes

The authors declare no competing financial interest.

■ ACKNOWLEDGMENTS

The authors thank Robby Prang (KNMF, KIT) for assistance with the SEM and FIB sample preparation, Professor Paul J. Ragogna (Western) for access to TGA and Raman instruments, Professor Robert H. E. Hudson (Western) for access to spectrofluorometer, Professor Martin J. Stillman and Dr. Chris Levy (Western) for access and assistance with low-temperature photoluminescence measurements, Kim Law (Stable Isotope Laboratory, Department of Earth Sciences, Western) for assistance with PXRD and Ying Zhang (Western Advanced Analysis and Materials Testing Laboratory, Engineering Department, Western) for assistance with UV−vis diffuse reflectance spectroscopy.

■ REFERENCES

(1) Vanmaekelbergh, D. *Nano Today* **2011**, *6* (4), 419.
(2) Gao, Y.; Tang, Z. *Small* **2011**, *7* (15), 2133.
(3) Talapin, D. V. *MRS Bull.* **2012**, *37* (1), 63.
(4) Hanrath, T. *J. Vac. Sci. Technol., A* **2012**, *30* (3), 30802.
(5) Huang, M. H.; Thoka, S. *Nano Today* **2015**, *10* (1), 81.
(6) Xu, L.; Ma, W.; Wang, L.; Xu, C.; Kuang, H.; Kotov, N. A. *Chem. Soc. Rev.* **2013**, *42* (7), 3114.
(7) Talapin, D. V.; Lee, J.-S.; Kovalenko, M. V.; Shevchenko, E. V. *Chem. Rev.* **2010**, *110* (1), 389.
(8) Nozik, A. J.; Beard, M. C.; Luther, J. M.; Law, M.; Ellingson, R. J.; Johnson, J. C. *Chem. Rev.* **2010**, *110* (11), 6873.
(9) Yang, J.; Choi, M. K.; Kim, D.-H.; Hyeon, T. *Adv. Mater.* **2016**, *28* (6), 1176.
(10) Collier, C. P.; Vossmeyer, T.; Heath, J. R. *Annu. Rev. Phys. Chem.* **1998**, *49*, 371.
(11) Bishop, K. J. M.; Wilmer, C. E.; Soh, S.; Grzybowski, B. A. *Small* **2009**, *5* (14), 1600.
(12) Zheng, N. F.; Bu, X. H.; Lu, H. W.; Zhang, Q. C.; Feng, P. Y. *J. Am. Chem. Soc.* **2005**, *127* (34), 11963.
(13) Bendova, M.; Puchberger, M.; Schubert, U. *Eur. J. Inorg. Chem.* **2010**, *2010* (21), 3299.
(14) Vossmeyer, T.; Reck, G.; Schulz, B.; Katsikas, L.; Weller, H. *J. Am. Chem. Soc.* **1995**, *117* (51), 12881.
(15) Feng, P.; Bu, X.; Zheng, N. *Acc. Chem. Res.* **2005**, *38* (4), 293.
(16) Yang, X.-L.; Zhang, J.; Ren, S.-B.; Li, Y.-Z.; Huang, W.; Du, H.-B.; You, X.-Z. *Inorg. Chem. Commun.* **2010**, *13* (11), 1337.
(17) Vossmeyer, T.; Reck, G.; Katsikas, L.; Haupt, E.; Schulz, B.; Weller, H. *Science* **1995**, *267* (5203), 1476.
(18) Niederberger, M.; Cölfen, H. *Phys. Chem. Chem. Phys.* **2006**, *8* (28), 3271.
(19) Zhang, Q.; Liu, S.-J.; Yu, S.-H. *J. Mater. Chem.* **2009**, *19* (2), 191.
(20) Bahrig, L.; Hickey, S. G.; Eychmüller, A. *CrystEngComm* **2014**, *16* (40), 9408.
(21) Lu, C.; Tang, Z. *Adv. Mater.* **2016**, *28* (6), 1096.
(22) De Yoreo, J. J.; Gilbert, P. U. P. A.; Sommerdijk, N. A. J. M.; Penn, R. L.; Whitelam, S.; Joester, D.; Zhang, H.; Rimer, J. D.; Navrotsky, A.; Banfield, J. F.; Wallace, A. F.; Michel, F. M.; Meldrum, F. C.; Cölfen, H.; Dove, P. M. *Science* **2015**, *349* (6247), aaa6760.
(23) Tang, Z. Y.; Kotov, N. A.; Giersig, M. *Science* **2002**, *297* (5579), 237.
(24) Cho, K. S.; Talapin, D. V.; Gaschler, W.; Murray, C. B. *J. Am. Chem. Soc.* **2005**, *127* (19), 7140.
(25) Koh, W.; Bartnik, A. C.; Wise, F. W.; Murray, C. B. *J. Am. Chem. Soc.* **2010**, *132* (11), 3909.
(26) Li, Z.; Sui, J.; Li, X.; Cai, W. *Langmuir* **2011**, *27* (6), 2258.
(27) Sarkar, S.; Acharya, S.; Chakraborty, A.; Pradhan, N. *J. Phys. Chem. Lett.* **2013**, *4* (19), 3292.
(28) Wang, Z.; Schliehe, C.; Wang, T.; Nagaoka, Y.; Cao, Y. C.; Bassett, W. A.; Wu, H.; Fan, H.; Weller, H. *J. Am. Chem. Soc.* **2011**, *133* (37), 14484.
(29) Boneschanscher, M. P.; Evers, W. H.; Geuchies, J. J.; Altantzis, T.; Goris, B.; Rabouw, F. T.; van Rossum, S. a. P.; van der Zant, H. S. J.; Siebbeles, L. D. A.; Van Tendeloo, G.; Swart, I.; Hilhorst, J.; Petukhov, A. V.; Bals, S.; Vanmaekelbergh, D. *Science* **2014**, *344* (6190), 1377.
(30) Sanchez, C.; Soler-Illia, G.; Ribot, F.; Lalot, T.; Mayer, C. R.; Cabuil, V. *Chem. Mater.* **2001**, *13* (10), 3061.
(31) Cheetham, A. K.; Rao, C. N. R.; Feller, R. K. *Chem. Commun.* **2006**, No. 46, 4780.
(32) Vaqueiro, P. *Dalton Trans.* **2010**, *39* (26), 5965.
(33) Zhang, Q.; Bu, X.; Lin, Z.; Wu, T.; Feng, P. *Inorg. Chem.* **2008**, *47* (21), 9724.
(34) Chen, Z.; Luo, D.; Luo, X.; Kang, M.; Lin, Z. *Dalton Trans.* **2012**, *41* (14), 3942.
(35) Zheng, N. F.; Bu, X. H.; Lu, H. W.; Chen, L.; Feng, P. Y. *J. Am. Chem. Soc.* **2005**, *127* (43), 14990.
(36) Zheng, N.; Bu, X.; Lauda, J.; Feng, P. *Chem. Mater.* **2006**, *18* (18), 4307.
(37) Kagan, C. R.; Murray, C. B. *Nat. Nanotechnol.* **2015**, *10* (12), 1013.
(38) Garcia-Rodriguez, R.; Hendricks, M. P.; Cossairt, B. M.; Liu, H.; Owen, J. S. *Chem. Mater.* **2013**, *25* (8), 1233.

DOI: 10.1021/jacs.6b10490
J. Am. Chem. Soc. 2017, 139, 1129−1144

(39) Lee, G. S. H.; Craig, D. C.; Ma, I.; Scudder, M. L.; Bailey, T. D.; Dance, I. G. *J. Am. Chem. Soc.* **1988**, *110* (14), 4863.
(40) Eichhöfer, A.; Hampe, O. *J. Cluster Sci.* **2007**, *18* (3), 494.
(41) Herron, N.; Calabrese, J.; Farneth, W.; Wang, Y. *Science* **1993**, *259* (5100), 1426.
(42) Behrens, S.; Bettenhausen, M.; Deveson, A. C.; Eichhöfer, A.; Fenske, D.; Lohde, A.; Woggon, U. *Angew. Chem., Int. Ed. Engl.* **1996**, *35* (19), 2215.
(43) Soloviev, V. N.; Eichhöfer, A.; Fenske, D.; Banin, U. *J. Am. Chem. Soc.* **2000**, *122* (11), 2673.
(44) Beecher, A. N.; Yang, X.; Palmer, J. H.; LaGrassa, A. L.; Juhas, P.; Billinge, S. J. L.; Owen, J. S. *J. Am. Chem. Soc.* **2014**, *136* (30), 10645.
(45) Matheis, K.; Eichhöfer, A.; Weigend, F.; Ehrler, O. T.; Hampe, O.; Kappes, M. M. *J. Phys. Chem. C* **2012**, *116* (25), 13800.
(46) Soloviev, V. N.; Eichhöfer, A.; Fenske, D.; Banin, U. *J. Am. Chem. Soc.* **2001**, *123* (10), 2354.
(47) Warren, B. E. *X-ray diffraction*; Addison-Wesley series in metallurgy and materials; Addison-Wesley Pub. Co.: Reading, MA, 1969.
(48) Klug, H. P.; Alexander, L. E. *X-ray diffraction procedures for polycrystalline and amorphous materials*, 2nd ed.; Wiley: New York, 1974.
(49) Morris-Cohen, A. J.; Malicki, M.; Peterson, M. D.; Slavin, J. W. J.; Weiss, E. A. *Chem. Mater.* **2013**, *25* (8), 1155.
(50) *Landolt-Börnstein: Numerical Data and Functional Relationships in Science and Technology - New Series. II-VI and I-VII Compounds; Semimagnetic Compounds*; Rössler, U., Ed.; Condensed Matter; Springer: Berlin, 1999; *Vol. 41B*.
(51) Rolo, A. G.; Vasilevskiy, M. I. *J. Raman Spectrosc.* **2007**, *38* (6), 618.
(52) Lin, C.; Kelley, D. F.; Rico, M.; Kelley, A. M. *ACS Nano* **2014**, *8* (4), 3928.
(53) Richter, H.; Wang, Z. P.; Ley, L. *Solid State Commun.* **1981**, *39* (5), 625.
(54) Campbell, I. H.; Fauchet, P. M. *Solid State Commun.* **1986**, *58* (10), 739.
(55) Trallero-Giner, C.; Debernardi, A.; Cardona, M.; Menendez-Proupin, E.; Ekimov, A. I. *Phys. Rev. B: Condens. Matter Mater. Phys.* **1998**, *57* (8), 4664.
(56) Dzhagan, V. M.; Valakh, M. Y.; Raevskaya, A. E.; Stroyuk, A. L.; Kuchmiy, S. Y.; Zahn, D. R. T. *Nanotechnology* **2008**, *19* (30), 305707.
(57) Nien, Y.-T.; Zaman, B.; Ouyang, J.; Chen, I.-G.; Hwang, C.-S.; Yu, K. *Mater. Lett.* **2008**, *62* (30), 4522.
(58) Lin, C.; Gong, K.; Kelley, D. F.; Kelley, A. M. *J. Phys. Chem. C* **2015**, *119* (13), 7491.
(59) Ueyama, N.; Sugawara, T.; Sasaki, K.; Nakamura, A.; Yamashita, S.; Wakatsuki, Y.; Yamazaki, H.; Yasuoka, N. *Inorg. Chem.* **1988**, *27* (4), 741.
(60) Levchenko, T. I.; Kübel, C.; Wang, D.; Najafabadi, B. K.; Huang, Y.; Corrigan, J. F. *Chem. Mater.* **2015**, *27* (10), 3666.
(61) Bendova, M.; Puchberger, M.; Pabisch, S.; Peterlik, H.; Schubert, U. *Eur. J. Inorg. Chem.* **2010**, *2010* (15), 2266.
(62) Alivisatos, A. P.; Harris, A. L.; Levinos, N. J.; Steigerwald, M. L.; Brus, L. E. *J. Chem. Phys.* **1988**, *89* (7), 4001.
(63) Bawendi, M. G.; Wilson, W. L.; Rothberg, L.; Carroll, P. J.; Jedju, T. M.; Steigerwald, M. L.; Brus, L. E. *Phys. Rev. Lett.* **1990**, *65* (13), 1623.
(64) Ekimov, A. I.; Hache, F.; Schanneklein, M. C.; Ricard, D.; Flytzanis, C.; Kudryavtsev, I. A.; Yazeva, T. V.; Rodina, A. V.; Efros, A. L. *J. Opt. Soc. Am. B* **1993**, *10* (1), 100.
(65) Yu, W. W.; Qu, L. H.; Guo, W. Z.; Peng, X. G. *Chem. Mater.* **2003**, *15* (14), 2854.
(66) Eichhöfer, A.; Aharoni, A.; Banin, U. *Z. Anorg. Allg. Chem.* **2002**, *628* (11), 2415.
(67) Gong, K.; Zeng, Y.; Kelley, D. F. *J. Phys. Chem. C* **2013**, *117* (39), 20268.
(68) Reichardt, C.; Welton, T. *Solvents and solvent effects in organic chemistry*, 4th ed.; Wiley-VCH: Weinheim, 2010.
(69) Bawendi, M. G.; Carroll, P. J.; Wilson, W. L.; Brus, L. E. *J. Chem. Phys.* **1992**, *96* (2), 946.
(70) Hoheisel, W.; Colvin, V. L.; Johnson, C. S.; Alivisatos, A. P. *J. Chem. Phys.* **1994**, *101* (10), 8455.
(71) Norris, D. J.; Bawendi, M. G. *J. Chem. Phys.* **1995**, *103* (13), 5260.
(72) Norris, D. J.; Efros, A. L.; Rosen, M.; Bawendi, M. G. *Phys. Rev. B: Condens. Matter Mater. Phys.* **1996**, *53* (24), 16347.
(73) Norris, D. J.; Sacra, A.; Murray, C. B.; Bawendi, M. G. *Phys. Rev. Lett.* **1994**, *72* (16), 2612.
(74) Norris, D. J.; Bawendi, M. G. *Phys. Rev. B: Condens. Matter Mater. Phys.* **1996**, *53* (24), 16338.
(75) Brus, L. *IEEE J. Quantum Electron.* **1986**, *22* (9), 1909.
(76) Henglein, A. *Chem. Rev.* **1989**, *89* (8), 1861.
(77) Bowers, M. J.; McBride, J. R.; Rosenthal, S. J. *J. Am. Chem. Soc.* **2005**, *127* (44), 15378.
(78) Aharoni, A.; Eichhöfer, A.; Fenske, D.; Banin, U. *Opt. Mater.* **2003**, *24* (1−2), 43.
(79) Soloviev, V. N.; Eichhofer, A.; Fenske, D.; Banin, U. *Phys. Status Solidi B* **2001**, *224* (1), 285.
(80) Chestnoy, N.; Harris, T. D.; Hull, R.; Brus, L. E. *J. Phys. Chem.* **1986**, *90* (15), 3393.
(81) Klimov, V. I.; Mikhailovsky, A. A.; McBranch, D. W.; Leatherdale, C. A.; Bawendi, M. G. *Science* **2000**, *287* (5455), 1011.
(82) Mork, A. J.; Weidman, M. C.; Prins, F.; Tisdale, W. A. *J. Phys. Chem. C* **2014**, *118* (25), 13920.
(83) Morello, G.; De Giorgi, M.; Kudera, S.; Manna, L.; Cingolani, R.; Anni, M. *J. Phys. Chem. C* **2007**, *111* (16), 5846.
(84) Sharma, S. N.; Pillai, Z. S.; Kamat, P. V. *J. Phys. Chem. B* **2003**, *107* (37), 10088.
(85) As all known tetrahedral CdE nanoclusters belong to a particular series where each member has a defined stoichiometry, it is convenient to identify such nanoclusters by the number of Cd atoms.
(86) Nguyen, K. A.; Pachter, R.; Day, P. N.; Su, H. *J. Chem. Phys.* **2015**, *142* (23), 234305.
(87) Buckley, J. J.; Couderc, E.; Greaney, M. J.; Munteanu, J.; Riche, C. T.; Bradforth, S. E.; Brutchey, R. L. *ACS Nano* **2014**, *8* (3), 2512.
(88) Dolai, S.; Dass, A.; Sardar, R. *Langmuir* **2013**, *29* (20), 6187.
(89) Boles, M. A.; Ling, D.; Hyeon, T.; Talapin, D. V. *Nat. Mater.* **2016**, *15* (2), 141.
(90) Bawendi, M. G.; Kortan, A. R.; Steigerwald, M. L.; Brus, L. E. *J. Chem. Phys.* **1989**, *91* (11), 7282.
(91) Ingham, B. *Crystallogr. Rev.* **2015**, *21* (4), 229.
(92) Unlike this, the Cd/Se atomic ratio for **1** was found to be essentially smaller (0.74:1) which reflects the presence of nanocluster constituents having anionic facets.
(93) Meyns, M.; Iacono, F.; Palencia, C.; Geweke, J.; Coderch, M. D.; Fittschen, U. E. A.; Gallego, J. M.; Otero, R.; Juarez, B. H.; Klinke, C. *Chem. Mater.* **2014**, *26* (5), 1813.
(94) Adams, R. D.; Zhang, B.; Murphy, C. J.; Yeung, L. K. *Chem. Commun.* **1999**, No. 4, 383.
(95) Greaney, M. J.; Couderc, E.; Zhao, J.; Nail, B. A.; Mecklenburg, M.; Thornbury, W.; Osterloh, F. E.; Bradforth, S. E.; Brutchey, R. L. *Chem. Mater.* **2015**, *27* (3), 744.
(96) Kim, W. D.; Kim, J.-H.; Lee, S.; Lee, S.; Woo, J. Y.; Lee, K.; Chae, W.-S.; Jeong, S.; Bae, W. K.; McGuire, J. A.; Moon, J. H.; Jeong, M. S.; Lee, D. C. *Chem. Mater.* **2016**, *28* (3), 962.
(97) Levchenko, T. I.; Kübel, C.; Huang, Y.; Corrigan, J. F. *Chem. - Eur. J.* **2011**, *17* (51), 14394.
(98) Nogami, M.; Koike, R.; Jalem, R.; Kawamura, G.; Yang, Y.; Sasaki, Y. *J. Phys. Chem. Lett.* **2010**, *1* (2), 568.
(99) Cao, Y.; Yang, Y.; Shan, Y.; Fu, C.; Long, N. V.; Huang, Z.; Guo, X.; Nogami, M. *Nanoscale* **2015**, *7* (46), 19461.
(100) Antonietti, M.; Ozin, G. A. *Chem. - Eur. J.* **2004**, *10* (1), 28.
(101) Kanatzidis, M. G. *Adv. Mater.* **2007**, *19* (9), 1165.
(102) Shi, Y.; Wan, Y.; Zhao, D. *Chem. Soc. Rev.* **2011**, *40* (7), 3854.
(103) Liu, X.; Hu, R.; Chai, L.; Li, H.; Gu, J.; Qian, Y. *J. Nanosci. Nanotechnol.* **2009**, *9* (4), 2715.

DOI: 10.1021/jacs.6b10490
J. Am. Chem. Soc. 2017, 139, 1129−1144

(104) Chu, L.; Zhou, B.; Mu, H.; Sun, Y.; Xu, P. *J. Cryst. Growth* **2008**, *310* (24), 5437.
(105) Kumar, P.; Singh, K.; Srivastava, O. N. *J. Cryst. Growth* **2010**, *312* (19), 2804.
(106) Zhang, X.; Zhang, D.; Tang, H.; Ji, X.; Zhang, Y.; Tang, G.; Li, C. *Mater. Res. Bull.* **2014**, *53*, 96.
(107) Castro-Guerrero, C. F.; Deepak, F. L.; Ponce, A.; Cruz-Reyes, J.; Del Valle-Granados, M.; Fuentes-Moyado, S.; Galvan, D. H.; Jose-Yacaman, M. *Catal. Sci. Technol.* **2011**, *1* (6), 1024.
(108) Wang, J.; Feng, H.; Chen, K.; You, T. *Mater. Lett.* **2013**, *104*, 87.
(109) Lang, D.; Liu, F.; Qiu, G.; Feng, X.; Xiang, Q. *ChemPlusChem* **2014**, *79* (12), 1726.
(110) Park, K. H.; Jang, K.; Son, S. U. *Angew. Chem., Int. Ed.* **2006**, *45* (28), 4608.
(111) Zhu, Y.; Chen, Y.; Liu, L. *J. Cryst. Growth* **2011**, *328* (1), 70.
(112) Wang, W. Z.; Poudel, B.; Yang, J.; Wang, D. Z.; Ren, Z. F. *J. Am. Chem. Soc.* **2005**, *127* (40), 13792.
(113) Shi, W.; Zhou, L.; Song, S.; Yang, J.; Zhang, H. *Adv. Mater.* **2008**, *20* (10), 1892.
(114) Schulz, S.; Heimann, S.; Friedrich, J.; Engenhorst, M.; Schierning, G.; Assenmacher, W. *Chem. Mater.* **2012**, *24* (11), 2228.
(115) Liang, Y.; Wang, W.; Zeng, B.; Zhang, G.; Huang, J.; Li, J.; Li, T.; Song, Y.; Zhang, X. *J. Alloys Compd.* **2011**, *509* (16), 5147.
(116) Ren, W.; Cheng, C.; Xu, Y.; Ren, Z.; Zhong, Y. *J. Alloys Compd.* **2010**, *501* (1), 120.
(117) Hanifehpour, Y.; Joo, S. W. *J. Nanomater.* **2014**, *2014*, 452659.
(118) Saltzmann, T.; Bornhoefft, M.; Mayer, J.; Simon, U. *Angew. Chem., Int. Ed.* **2015**, *54* (22), 6632.
(119) Talapin, D. V.; Shevchenko, E. V.; Kornowski, A.; Gaponik, N.; Haase, M.; Rogach, A. L.; Weller, H. *Adv. Mater.* **2001**, *13* (24), 1868.
(120) Cölfen, H.; Antonietti, M. *Angew. Chem., Int. Ed.* **2005**, *44* (35), 5576.
(121) Zhang, H.; De Yoreo, J. J.; Banfield, J. F. *ACS Nano* **2014**, *8* (7), 6526.
(122) Zhou, L.; O'Brien, P. *Small* **2008**, *4* (10), 1566.
(123) Thanh, N. T. K.; Maclean, N.; Mahiddine, S. *Chem. Rev.* **2014**, *114* (15), 7610.
(124) Liu, Y.; Wang, D.; Peng, Q.; Chu, D.; Liu, X.; Li, Y. *Inorg. Chem.* **2011**, *50* (12), 5841.
(125) Dutta, S.; Wu, K. C.-W.; Kimura, T. *Chem. Mater.* **2015**, *27* (20), 6918.

DOI: 10.1021/jacs.6b10490
J. Am. Chem. Soc. 2017, 139, 1129−1144